UK Atomic Energy Authority

UKAEA-STEP-PR(23)14

A. Kirschner, S.S. Henderson, S. Brezinsek, J. Romazanov, M. Kovari, C. Baumann, Ch. Linsmeier, E. Flynn, J. Hess, R.T. Osawa, S.L. Newton, D. Moulton

# Erosion estimates for the divertor and main wall components from STEP

# Erosion estimates for the divertor and main wall components from STEP

A. Kirschner, S.S. Henderson, S. Brezinsek, J. Romazanov, M. Kovari, C. Baumann, Ch. Linsmeier, E. Flynn, J. Hess, R.T. Osawa, S.L. Newton, D. Moulton

This is a preprint of a paper submitted for publication in Nuclear Fusion

# Erosion estimates for the divertor and main wall components from STEP

A. Kirschner[1], S.S. Henderson[2], S. Brezinsek[1], J. Romazanov[1], M. Kovari[2], C. Baumann[1], Ch. Linsmeier[1], E. Flynn[2], J. Hess[2], R.T. Osawa[2], S.L. Newton[2], D. Moulton[2] and the STEP Team

*[1]Forschungszentrum Jülich GmbH, Institut für Energie- und Klimaforschung - Plasmaphysik, 52425 Jülich, Germany*

*[2]Culham Science Centre, United Kingdom Atomic Energy Authority, Abingdon, OX14 3DB, UK*

E-mail: a.kirschner@fz-juelich.de

**Abstract**

The tungsten erosion within STEP assuming tungsten main wall and tungsten divertor has been estimated with ERO at the inner and outer divertor, at the inner and outer midplane and at the outboard baffle entrance. Plasma parameters are based on SOLPS simulations applying argon puffing for edge cooling. The modelled peak gross erosion is highest within the divertor with up to 1E19 W /$m^2$/s within the inner and 7E19 W /$m^2$/s in the outer one for the plasma parameter range studied. At the main wall the gross erosion is about 2E18 W /$m^2$/s at the inner midplane and 1.3E17 W /$m^2$/s at the outer one. However, tungsten deposition within the divertor is much larger with amounts between 88% and 98% and only between 10% and 60% at the midplane. At all locations studied, tungsten erosion due to deuterium ions is negligibly small compared to the erosion by argon ions. Erosion due to deuterium atoms has been studied for the outer midplane and is there at least four times smaller than the erosion due to argon ions.

Keywords: STEP, plasma-wall interaction, erosion, deposition, tungsten, ERO, SOLPS

## 1. Introduction

The Spherical Tokamak for Energy Production (STEP) will be a prototype fusion energy plant targeting ~2040 to serve as a path to the commercial viability of fusion. The project is currently in its concept design phase aiming to have a fully evolved design and approval to build around 2032. The STEP prototype reactor is expected to be a 100 MW power station with a total diameter of only around 10 m. The spherical shape enables a compact design and improves efficiency in the magnetic field and potentially reduces the plant´s costs. Moreover, a spherical tokamak can achieve much higher beta values than conventional tokamaks, which is beneficial for the achievement of improved confinement. As first wall material currently tungsten is the preferred option for the main wall and the divertor with liquid components under discussion. More details about the STEP project, advantages but also challenges of the spherical tokamak concept can be found in [1] and references therein.

In the following, estimates of gross erosion and resulting net erosion/deposition at various wall components in STEP will be provided for a range of steady state ELM-averaged plasma conditions with semi-detached divertor. Transient events are not considered. The plasma conditions are in line with power load limits of the wall components. The erosion/deposition estimates will be used to draw conclusions about the life time of the wall components. The gross erosion, impurity transport and subsequent deposition is calculated with the 3D Monte Carlo code ERO [2] for the inner and outer divertor targets, inner and outer midplane wall tiles and the outboard baffle entrance. As wall material only tungsten is considered - whereas liquid surfaces are disregarded - and the main plasma impurity is argon originating from gas injection. The plasma parameters used for the simulations are based on SOLPS [3, 4] modelling for the STEP device. A certain set of plasma scenarios is applied to study the effect of varying plasma parameters. Also the influence of the anomalous cross field diffusion coefficient assumed for the ERO simulations is analysed by means of a parameter study. The shape of the wall elements in ERO is simplified neglecting possible curvatures or recessed areas like gaps or castellations. Surface roughness is not treated in the current modelling but could be addressed in future studies.

## 2. The ERO code

The simulations presented are carried out with the 3D Monte-Carlo code ERO [2], which models the migration of impurities within the edge of a plasma in a fusion device and considers various plasma-wall interaction processes. Within a given plasma background (electron and ion temperature, density, parallel flow velocity, magnetic field) ERO simulates gross erosion of wall components dependent on the incoming particle flux of ions and atoms. Physical sputtering yields depend on the projectiles´ impact energy and angle. In the present work, new sputter yields for tungsten by background deuterium and argon ions have been calculated with SDTrimSP [5] assuming Maxwell energy distribution and considering a sheath potential of $3T_e$, with $T_e$ the electron temperature. For the impact angle a mean value of 60° is assumed [6, 7]. The resulting yields are presented in chapter 3. Sputtering by background neutral deuterium atoms can be included if the necessary input values for flux, impact energy and angle distribution are available. Sputtered particles leave the surface as neutrals with cosine angular and Thompson energy distribution (around surface binding energy), following straight trajectories. Depending on the local plasma parameters, ionisation takes place (probability calculated with Monte-Carlo method using ionisation rate coefficients from [8]) and ERO considers the Lorentz force in a combined electric/magnetic field with full gyration, friction with background plasma and thermal force as correction term. The parallel flow velocity of background plasma ions, necessary to determine the

friction force, is calculated based on a 1D edge plasma model as described in [2, 9, 10] leading to acoustic sound speed near the target surface and zero flow velocity at the stagnation point. For the thermal force only the ions are considered as they typically dominate. The ion temperature gradient along the magnetic field is calculated according a simple SOL model as described in [9]. Anomalous cross field diffusion can be included, variations of the cross field diffusion coefficient will be studied. Part of the eroded particles return to the surface, where they can be deposited, reflected (with reflection coefficients according to TRIM [11]) and erode further material. The erosion due to returning particles is calculated by means of the Eckstein fit formula [12], which provides the sputter yield in dependence on impact energy and angle - the latter are calculated by ERO as result of the particle trajectory ending at the surface wherefore in contrast to the erosion due to background species no pre-calculated yields are necessary. Reflected particles are re-launched into the plasma in a repetitive manner until deposition or leaving the simulation volume. As main result, ERO provides profiles along the considered wall components of gross and net erosion and density and light emission of impurities within the simulation volume. ERO has been benchmarked against many experiments (e.g. [13-30]) and used to predict the lifetime of wall components in ITER (e.g. [31-34]).
The ERO simulations are performed within a localised simulation volume assuming toroidal symmetry with periodic boundary conditions in toroidal direction. A constant magnetic field is assumed within the simulation volume. In addition to the sheath electric field, further contributions (radial electric field and parallel electric fields) are considered. Details about the calculation of the electric fields are described e.g. in [2, 9, 10]. Simulations are done in the test particle approximation, which means that the background plasma is not influenced by the sputtered particles. The shape of the wall elements in ERO is simplified neglecting possible curvatures or recessed areas like gaps or castellations. Surface roughness is not treated at the moment but could be addressed in future studies.

## 3. Tungsten sputter yields

As mentioned before, sputtering by traced particles is calculated using the fit formula for sputter yields according to [12]. Background species are not followed within the ERO simulations and therefore pre-calculated sputter yields are needed. For the current work sputter yields have been calculated with SDTrimSP for deuterium and argon ion impact on tungsten, argon is the only impurity species considered in the following. As the SOLPS [3] based plasma parameter used for the STEP simulations typically show ion temperatures $T_i$ larger than the electron temperatures $T_e$, yields have been calculated for various values of the ratio of $T_i/T_e$. The SDTrimSP simulations have been done for Maxwell distributed projectiles around $T_i$, in addition a sheath potential of $3T_e$ has been considered. A mean impact angle of 60° is assumed for the deuterium and argon ions. This assumption is widely used in plasma-wall interaction modelling codes and also confirmed by special ERO simulations for various conditions, see e.g. [6, 7]. Only singly ionised argon is taken into account. Figure 1 summarises the resulting yields as function of the electron temperature for different values of $T_i/T_e$.
It can be seen that tungsten sputtering by deuterium ions is negligible at electron temperatures below about 20 eV if $T_i/T_e$ is not larger than 2. However, even with an electron temperature of 20 eV and $T_i/T_e = 6$, the sputter yield is comparably small and not greater than 0.07%. Sputtering of tungsten by argon ions is much more effective and yields in the percent range occur already at electron temperatures of a few eV if $T_i/T_e$ is larger than about 4. For the plasma conditions, which will be studied later on, one can conclude, that tungsten sputtering is strongly dominated or even

solely determined by argon ions and not deuterium ions. In contrast to deuterium ions, sputtering due to CX deuterium neutrals may significantly contribute to the overall erosion if their energy (and flux) is large enough - this will be studied in more detail in section 4.3 exemplarily for the erosion at the midplane region of STEP.
Within the ERO simulations the sputter yields by background D and Ar ions are determined by 2D interpolation between the discrete values of $T_e$ and $T_i/T_e$ provided in figure 1. Outside the range of available data the nearest data points are taken.

## 4. ERO simulations

As the STEP project is currently in its design phase there is no final geometry of the machine available. For the ERO simulations the status quo from a certain time has been taken as a basis and in particular according SOLPS plasma background simulations existing at that time have been used as input.
The ERO simulations presented here are divided into time steps of $\Delta T = 0.1$s. As particles sputtered within a certain time step are traced within the succeeding time step, several time steps are necessary to reach steady state. Typically it is seen that already after a few steps constant surface-integrated rates are obtained and thus steady state conditions have been reached. Also the time evolution of tungsten gross-erosion, self-sputtering and deposition at individual surface cells show a similar behaviour except of locations at small fluxes (e.g. farer away from the strike points at the divertor targets), where a certain scattering is unavoidable. In general, for the simulations presented here ten simulation steps are sufficient and thus normally the results of the 10th time step are shown. For the simulations 20 test particles are launched from each surface cell within each time step. With that choice the computational time is within reasonable limits and the statistics is still sufficient.

### 4.1. Outer divertor

#### 4.1.1 Basic set-up for the outer divertor: simulation volume and magnetic field

Figure 2 a) shows the poloidal cross section of the lower divertor region including the magnetic flux surfaces (in blue) of an example case. As the upper and lower divertors are quite symmetric with respect to the plasma conditions, the ERO simulations are restricted to the lower divertor. The simulation volume to be used for the ERO simulations for the outer divertor is indicated in figure 2 a) and shown enlarged in figure 2 c). The x-axis corresponds to the major radius and the z-axis to the height of the STEP coordinates of figure 2 a). The "ERO coordinate" x = 0 mm (roughly) corresponds to x = 0 m from the SOLPS target plasma profiles. Negative x-values on the target are within the PFR, positive ones within the SOL. In toroidal direction (y-axis, perpendicular to the (x,z)-plane) the simulation volume has a size of 16 m. Within the ERO simulation volume the magnetic flux surfaces are assumed to be parallel and having an angle of $\alpha_{sep} = 15°$ with the target surface, see figure 2 c). Along the x-axis the target surface is divided into 200 cells of 2 mm length, along the y-axis only two cells each of 8 m length are used.
As the plasma parameters are assumed to be symmetric in toroidal direction (i.e. constant) the simulations are done with quasi-periodic boundary conditions in that direction. For that purpose the length of the simulation volume in toroidal direction has been chosen with 16 m large enough to avoid particle losses in that direction. All profiles along the x-direction of erosion and deposition will be averaged over the two toroidal cells. For the output of the 2D distribution of sputtered tungsten species above the target, the simulation volume is divided into cells of 1 mm length in x- and z-direction.

The magnetic field strength and direction are $B_{tot}$ = 1.81 T, $B_P$ = 0.93 T, and $B_T$ = 1.56 T. For the ERO simulations the magnetic field is assumed to be constant within the simulation volume. The angle $\alpha_B$ between the magnetic field and the surface is about 7.5°. The simulations with so-called "standard B" apply a magnetic field, which points out of the (x,z)-plane, whereas simulations with "reversed B" have a magnetic field pointing towards the (x,z)-plane. The connection length of 33 m for the outer divertor target is used in the ERO simulations.

### 4.1.2 Plasma parameter for the outer divertor

The electron temperature $T_e$ and density $n_e$ and the ion temperature $T_i$ based on SOLPS simulations are given as profiles along the target surface. Five different cases of plasma parameter are studied providing a scan of both electron and ion temperature. The argon concentration (assuming singly ionised $Ar^+$) for the different cases is provided by SOLPS and assumed to be constant within the ERO simulation volume. This simplification could introduce some significant uncertainty, however, simulations with spatially varying argon concentrations are out of the scope of the current work but will be performed in future studies. The plasma profiles are fitted by means of exponential functions with different decay lengths towards the scrape-off layer (SOL) and private-flux region (PFR) for $T_e$, $T_i$ and $n_e$. However, for the five different cases the same decay lengths are used. The target locations of the peak values for $T_e$, $T_i$ and $n_e$ are different for the five cases, which is taken into account in the simulations. The resulting plasma parameter profiles for the five different cases are presented in figure 3 using the ERO x-coordinate, which has been introduced in section 4.1.1. If the exponential fits reach a temperature of 1 eV or a density of 1E5 $cm^{-3}$ no further decrease is applied and the values are kept constant.
The peak values of the plasma parameters at the outer divertor plate are summarised in table 1. Also included in the table are the various decay lengths for the exponential fits of the plasma parameter and the Ar concentration for the different cases. It can be seen that higher Ar concentration in the divertor not always leads to smaller temperatures, for instance by comparing case 4 with case 5, which have same Ar puffing rates. The reason for this behaviour is that in case 4 the Ar puff is just below the X-point whereas in case 5 Ar is puffed directly into the inner and outer divertor. As result, similar puffing rates can lead to different plasma parameters depending on the puffing location.
It has to be noted that the quality of the exponential fits of the SOLPS plasma parameter profiles is different for the various cases. As example, figure 4 compares the original SOLPS profiles with the exponential fits for case 2 and case 5. For instance, it can be seen that the exponential fit of the electron temperature for case 5 results in a bit wider profile than the original SOLPS data both towards PFR and SOL. However, the approach of using exponential fit formula has the advantage that one can apply straight forward parameter variations of the decay lengths for further studies.
The ERO simulations need 2D distributed plasma parameters within the simulation volume. To extrapolate the target profiles into 2D, the following approach is made: The plasma parameters ($T_e$, $n_e$, $T_i$) are constant within the flux surfaces. For $T_e$, $n_e$ and $T_i$ the flux surface corresponding to the peak value is used to calculate the plasma parameter towards PFR and SOL by means of exponential decays. The decay is done perpendicular to that flux surface with decay lengths

$$\lambda_{2D\_PFR} = \lambda_{PFR} \cdot \sin(\alpha_{sep}) \quad (1a)$$

$$\lambda_{2D\_SOL} = \lambda_{SOL} \cdot \sin(\alpha_{sep}) \quad (1b)$$

with $\lambda_{PFR}$ and $\lambda_{SOL}$ the decay lengths according to table 1 and $\alpha_{sep}$ = 15° as introduced in section 4.1.1. Figure 5 shows exemplarily the resulting 2D electron temperature and density for case 5.

### 4.1.3 Simulations with "standard B" direction and no anomalous cross-field diffusion

The impinging deuterium ion flux is calculated in ERO by means of the following formula:

$$\Gamma_{D+} = n_e \cdot c_S \cdot \sin\alpha_B \quad (2)$$

with $c_S$ the acoustic sound speed depending on $T_e$ and $T_i$, and $\alpha_B = 7.5°$ the angle between the magnetic field and the surface. The resulting profiles are shown in figure 6 for the different cases under consideration. The peak flux varies between 1.3E24 ions/$m^2$/s for case 4 and 2.4E24 ions/$m^2$/s for case 3. The peak locations are at x = 33 mm for cases 1, 2, 3 and at x = 105 mm for cases 4, 5.

In the following the simulation results for the five cases are presented. The simulations are performed without cross-field diffusion and "standard" magnetic field direction as introduced in section 4.1.1. The effects of reversed B field and non-zero cross-field diffusion will be studied in sections 4.1.4. and 4.1.5. Figure 7 summarises the profiles of tungsten gross erosion, erosion by the background plasma ions, self-sputtering and deposition for the five cases. The different plasma parameters and argon concentrations (dominating eroding species) lead to different erosion, with the largest gross erosion peak in case 1 of about 6.7E19 W atoms/$m^2$/s and the smallest one in case 4 with about 5.1E16 W atoms/$m^2$/s. The comparably very small erosion in case 4 (although having comparably high electron and ion temperatures) is the result of the very small Ar divertor concentration in that case. Also case 2 shows relatively small gross erosion with a peak of about 3.1E17 W atoms/$m^2$/s, in that case due to the smallest electron and ion temperature. It can be summarised, that the gross erosion is a result of plasma parameters (defining the sputter yield and eroding flux) together with the amount of Ar ions as dominating eroding species in the plasma.

Tungsten deposition is determined by the electron density and temperature both governing the ionisation length of sputtered tungsten atoms. The surface-averaged amount of tungsten deposited on the target relative to the gross erosion varies between 83.2% for case 4 and 98.4% for case 3. The lowest deposition seen in case 4 is a result of relatively low electron density, only case 5 has even a bit lower density but compared to case 4 significantly larger electron temperature. Case 3 has the combination of large density and relatively large electron temperature and therefore shows the largest amount of deposition. The amount of surface-averaged tungsten self-sputtering relative to the overall tungsten gross erosion is between 26% and 46% with the lowest value in case 4 and the largest one in case 3 and thus a dependence on plasma condition resembling the amount of deposition. Table 2 summarises the values of peak gross erosion, amount of deposition, prompt deposition and self-sputtering for the five cases. The amount of prompt deposition is related to the overall deposition. Ions are counted as promptly deposited if their transport time until deposition is less than their gyration time.

For the cases 1, 2 and 3, tungsten particles, which are not deposited on the target mainly leave the simulation volume in z direction and a smaller part in plus x-direction towards the SOL. In the cases 4 and 5 with the smallest amounts of deposition, the main loss occurs in minus x-direction towards the PFR and smaller amounts in positive x- and z-direction. This observation suggests that in cases 4 and 5, having the smallest electron density and highest ion temperature, the thermal force can become important driving a significant amount of ions away from the surface. For the other conditions, the friction force towards the target is strongly dominating.

The profiles of net deposition/erosion rate resulting from deposition minus gross-erosion are presented in figure 8. Net deposition, i.e. growth of a tungsten layer, is shown with positive values and net erosion with negative ones. As expected from the gross erosion profiles, the values of peak net erosion differ quite strongly between the different cases with values ranging from about 0.3

nm/s for case 1 and 5E-4 nm/s for case 4. The values of the peak net erosion rate for all cases have been listed table 2. Within the SOL for all cases a region of net deposition occurs with maximum deposition rates between 0.2 nm/s for case 1 and 2E-4 nm/s for case 4.
The 2D distributions of tungsten atoms and charged ions are shown in figure 9 on the example of case 2 (having the smallest electron and ion temperature) and case 5 (largest electron and ion temperature). The figures clearly demonstrate the transport of ions along the magnetic field lines lying within the flux surfaces. This basic transport process along the magnetic field lines caused by the friction force with the background plasma leads to migration of W ions towards the SOL resulting in net deposition over there, see also figure 8. Also, the above-discussed increased loss of sputtered tungsten in minus x-direction for the cases with small electron density is seen by comparing the 2D W ion distributions for case 2 and case 5, the latter as an example for low density, high ion temperature and thus notable thermal force.

### 4.1.4 Reversed B field direction: outer divertor

The influence of a reversed magnetic field direction has been studied for the cases 2 and 5, with case 2 having the smallest electron and ion temperature and the largest electron density and case 5 having the largest electron and ion temperature and the smallest electron density.
Keeping the magnetic field strength unchanged, only the direction of the B field is changed by 180° resulting in a B field vector pointing towards the (x,z)-plane for the so-called "reversed B" condition. The reversed B field will alter the gyration direction of W ions and also the direction of the E×B drift. Typically, E×B drift effects resulting from the electric field within the sheath are not visible due to the very small thickness (in the sub-mm range) of the sheath. The E×B directions caused by the radial electric field within the outer divertor region for "standard B" and "reversed B" orientation are shown in figure 10. The radial electric field $E_{rad}$ is proportional to the gradient of the electron temperature and oriented antiparallel to the $T_e$ gradient, see [2] and references therein.
The modelled profiles of the tungsten net deposition/erosion rates are presented in figure 11 for case 2 and case 5 with reversed and standard B field direction. Anomalous cross-field diffusion is not considered in these simulations. In both cases it is seen that the deposition is shifted to the left towards the PFR applying the reversed B field direction. This results in reduced net erosion peaks and also in overall reduced net deposition rates within the SOL. The increased transport towards the PFR can be explained with the changed direction of the gyration. Also, the reversed B field leads to an E×B drift within the SOL directed towards the PFR. The overall amounts of tungsten deposition do not change significantly with reversed B (for case 2 increase from 93% to 96% and for case 5 decrease from 91% to 89%). The amounts of tungsten self-sputtering decrease in both cases with reversed B field (for case 2 from 27% to 22% and for case 5 from 34% to 25%). This can explained with the increased transport towards the PFR resulting in smaller impact energies of tungsten ions due to smaller electron and ion temperatures in that region. As for the standard B field, particles, which are not deposited, leave the simulation volume mainly in z-direction for case 2 and minus x-direction for case 5 with reversed B field.
The simulated distribution of ions above the target surface is for both cases 2 and 5 very similar with standard and reversed B field direction. Main changes in the tungsten ion transport due to the reversed B field occur rather near to the surface.

### 4.1.5 Consideration of anomalous cross-field diffusion: outer divertor

The simulations are performed with standard B field direction and considering anomalous cross-field diffusion coefficients $D_{perp}$ of 1 $m^2/s$ and 2 $m^2/s$ for case 2 and case 5. Compared to the

simulations shown so far, the integration time dt to calculate the test particle trajectories has been reduced by a factor of ten from 1E-9 to 1E-10 s. This has been done to reduce the displacement step of the test particle in space ($(6 \cdot D_{perp} \cdot dt)^{1/2}$) during each integration step due to the cross-field diffusion.
Figure 12 shows the resulting profiles of the net tungsten deposition/erosion along the outer divertor target. The profiles reveal increased deposition with increasing cross-field diffusion, in particular at the location of net erosion which results a reduction of the peak net erosion. Table 2 summarises the surface-averaged amounts of deposition and self-sputtering, both relative to the gross-erosion, the amount of prompt deposition relative to the overall deposition and the peak net erosion for the various cases. The amount of self-sputtering decreases with increasing anomalous diffusion coefficient. Tungsten ions returning to the target surface gain less energy from the friction with the background plasma when the cross-field diffusion is increased (as mentioned before the cross-field diffusion is calculated in ERO as a displacement step in space). This decreased impact energy finally reduces the self-sputtering yield.

### 4.2. Inner Divertor

#### 4.2.1 Basic set-up for the inner divertor: simulation volume and magnetic field

As for the outer divertor, the ERO simulations are restricted to the lower divertor since the upper and lower divertors are quite symmetric with respect to the plasma conditions. The simulation volume to be used for the ERO simulations is indicated in figure 2 a) and shown enlarged in figure 2 b) after rotating by 70° clockwise and mirroring at the target plane. The x-axis is along the inner target in "poloidal" direction and the z-axis is oriented perpendicular to the target. The "ERO coordinate" along the target reaches from x = -220 mm near the lower end of the target to x = +220 mm towards the upper end of the target. The "ERO coordinate" x= -115 mm (roughly) corresponds to x = 0 m from the target plasma profiles provided by SOLPS. As for the outer divertor simulations, in toroidal direction (y-axis, perpendicular to the (x,z)-plane) the simulation volume has a size of 16 m to enable quasi-periodic boundary conditions in that direction. The length of the simulation volume perpendicular to the target (z-direction) is 200 mm. Within the ERO simulation volume the magnetic flux surfaces are assumed to be parallel and having an angle of $\alpha_{sep} = 35°$ with the target surface, see figure 2 b). Along the x-axis the target surface is divided into 220 cells of 2 mm length, along the y-axis only two cells each of 8 m length are used.
As before, all profiles along the x-direction of erosion and deposition will be averaged over the two toroidal cells. For the output of the 2D distribution of sputtered tungsten species above the target, the simulation volume is divided into cells of 1 mm length in x- and z-direction.
The magnetic field strength and direction are $B_{tot} = 4.92$ T, $B_P = 0.64$ T, and $B_T = 4.88$ T. For the ERO simulations the magnetic field is assumed to be constant within the simulation volume. The angle $\alpha_B$ between the magnetic field and the surface is about 4°. The simulations with so-called "standard B" apply a magnetic field, which points towards the (x,z)-plane, whereas simulations with "reversed B" have a magnetic field pointing out of the (x,z)-plane. The connection length of 40 m for the inner divertor target is used in the ERO simulations.

#### 4.2.2 Plasma parameter for the inner divertor

The electron temperature $T_e$ and density $n_e$ and the ion temperature $T_i$ based on SOLPS simulations are given as profiles along the target surface. Three different cases of plasma parameter are studied. Also, the argon concentration (assuming singly ionised $Ar^+$) for the different cases is provided and assumed to be constant within the ERO simulation volume. Whereas for the outer divertor

simulations the target profiles have been fitted by exponential functions, such fitting is not reasonable for the inner target profiles. Therefore, the SOLPS data are imported directly by ERO. The resulting plasma parameter profiles for the different cases are presented in figure 13 using the ERO x-coordinate, which has been introduced in section 4.2.1. The peak values of the plasma parameters at the inner divertor plate are summarised in table 3. It is worth mentioning that the peaks are not found in the same location across the plate, see figure 13. Also included in the table are the Ar concentrations for the different cases. In case 0 the small Ar concentration leads to rather large electron and in particular ion temperatures in the scrape-off-layer. It has to be noted that the plasma parameters of case 2 are based on case 1, taking the same electron density profile but multiplying the profiles of the electron and ion temperature by a factor of 2.5. Case 2 represents a rough scaling of the SOLPS data for a slightly decreased argon concentration compared to case 1. As already mentioned before, the ERO simulations need 2D distributed plasma parameters within the simulation volume. To extrapolate the inner target profiles into 2D, the following approach is made: the plasma parameters ($T_e$, $n_e$, $T_i$) are constant within the flux surfaces. At a position (x,z) within the plasma, the plasma parameter from the projected position $x_0$ at the target is taken, the projection is done along the flux surfaces, see figure 14. Within the shaded region, indicated in figure 14, an exponential extrapolation of the plasma parameters is applied. Figure 15 shows exemplarily the resulting 2D electron temperature and density for case 1. The exponential decay lengths for the different cases are summarised in table 3. The decay lengths for the electron temperature are also used for the calculation of the radial electric field.

### 4.2.3 Simulations with "standard B" direction and no anomalous cross-field diffusion

The impinging deuterium ion flux is calculated according to equation (2) with $\alpha_B = 4°$ the angle between the magnetic field and the inner target surface. The resulting profiles are shown in figure 16 for the different cases under consideration. The peak fluxes are 9.6E23 ions/$m^2$/s for case 0, 7.5E23 ions/$m^2$/s for case 1, and 12E23 ions/$m^2$/s for case 2. The peak locations are located at about x = -95 mm for all three cases.

In the following the simulation results for the three cases are presented. The simulations are performed without cross-field diffusion and "standard" magnetic field direction as introduced in section 4.2.1. The effects of reversed B field and non-zero cross-field diffusion will be studied in subsequent sections 4.2.4 and 4.2.5 exemplarily for case 1. Figure 17 summarises the profiles of tungsten gross erosion, erosion by the background plasma ions, self-sputtering and deposition for the three cases. The different plasma parameters and argon concentrations (Ar is the dominating eroding species) lead to different erosion, with the largest gross erosion peak in case 0 of about 1.1E19 W atoms/$m^2$/s and the smallest one in case 1 with about 1.4E16 W atoms/$m^2$/s. The comparably small erosion in case 1 (although having largest Ar concentration) is the result of the smallest electron and ion temperatures and also the smallest electron densities. The opposite is true for case 0 having the largest peak electron and in particular very high peak ion temperature. Also, the highest electron density occurs in case 0. Altogether this leads to largest erosion although the Ar concentration is the smallest from the three cases. For all cases the Ar ions are the dominating eroding species in the plasma as the yields for tungsten erosion by deuterium ions are negligibly small for the plasma parameters considered.

Tungsten deposition is determined by the electron density and temperature both governing the ionisation length of sputtered tungsten atoms. The surface-averaged amount of tungsten deposited on the target relative to the gross erosion is 88.2% for case 1 and 98.6% for case 0 and case 2. The lowest deposition seen in case 1 is a result of relatively low electron and ion temperatures. The electron densities are very similar for the three different cases. The amount of surface-averaged

tungsten self-sputtering relative to the overall tungsten gross erosion is between 9% and 13% with the lowest value in case 1. These relatively small values result from comparably small impact energies of tungsten ions returning to the target taking place at locations away from the peak electron density. Therefore only limited energy gain due to friction with the background plasma occurs, resulting in impact energies, which are too low for more significant sputtering. Also the energy gain due to the sheath potential is small because of small electron and ion temperatures. Table 4 summarises the values of peak gross erosion, amount of deposition, prompt deposition and self-sputtering for the three cases. The amount of prompt deposition is given relative to the overall deposition. Ions are counted as promptly deposited if their transport time until deposition is less than their gyration time. The amount of prompt deposition is in all cases rather small with a minimum value of about only 5% in case 1. The peak of gross erosion is significantly away from the peak of maximum electron density, wherefore also the deposition occurs at locations with relatively small electron densities and in addition the electron temperatures are rather small resulting in small amounts of prompt deposition.
For the cases 0 and 2, tungsten particles, which are not deposited on the target mainly leave the simulation volume in plus x-direction towards the SOL. In case 1 nearly the same amount of tungsten particles leave the simulation volume in positive x- and z-direction. The small electron temperature in that case results in deeper penetration of sputtered tungsten into the plasma finally leading to significant losses towards the z-direction.
The profiles of net deposition/erosion rate resulting from deposition minus gross-erosion are presented in figure 18. Net deposition, i.e. growth of a tungsten layer, is shown with positive values and net erosion with negative ones. As expected from the gross erosion profiles, the values of peak net erosion differ quite strongly between the different cases with values ranging from about 1E-4 nm/s for case 1 and 0.04 nm/s for case 0. The values of the peak net erosion rate for all cases have been listed in table 4. For all cases a region of net deposition occurs within the SOL with maximum deposition rates between 1.5E-4 nm/s for case 1 and 0.06 nm/s for case 0.
The 2D distributions of tungsten atoms and charged ions are shown in figure 19 for the three cases. The figures clearly demonstrate the transport of ions along the magnetic field lines lying within the flux surfaces. This basic transport process caused by the friction force with the background plasma along the magnetic field lines leads to migration of W ions towards the PFR resulting in net deposition regions, see also figure 18. In addition, the above-discussed loss of sputtered tungsten in positive x-direction is seen and for case 1 the increased loss in z-direction is visible in the W atom distribution.

### 4.2.4 Reversed B field direction: inner divertor

Keeping the magnetic field strength unchanged, only the direction of the B field is changed by 180° resulting in a B field vector pointing out of the (x,z)-plane for the so-called "reversed B" condition. The reversed B field will alter the gyration direction of W ions and also the direction of the E×B drift. The E×B directions caused by the radial electric field within the inner divertor region for "standard B" and "reversed B" orientation are shown in figure 20. The radial electric field $E_{rad}$ is proportional to the gradient of the electron temperature and oriented antiparallel to the $T_e$ gradient, see [2] and references therein. The gradient of the electron temperature is calculated assuming the exponential decay lengths as summarised in table 3.
The modelled profiles of the tungsten net deposition/erosion rates are presented in figure 21 exemplarily for case 1 with reversed and standard B field direction. Anomalous cross-field diffusion is not considered in these simulations. It is seen that the net deposition peak is reduced with reversed B field direction. This can be explained with the changed direction of the gyration

leading to increased transport of eroded tungsten towards the SOL with reversed B. Effects due to the changed E×B direction are not very pronounced, also due to relatively small radial electric fields (as result from rather large exponential decay lengths of the electron temperature and also small electron temperatures) The overall amount of tungsten deposition does not change significantly with reversed B (decrease from 88.2% to 87.6%). The amount of tungsten self-sputtering slightly decreases with reversed B field (from 9.3% to 8.9%). As for the standard B field, particles, which are not deposited, leave the simulation volume in z-direction and positive x-direction.
The simulated distribution of ions above the target surface with reversed B field (not shown here) is very similar to the one with standard B direction. Main changes in the tungsten ion transport due to the reversed B field occur rather near to the surface.

### 4.2.5 Consideration of anomalous cross-field diffusion: inner divertor

The simulations are performed with standard B field direction and considering anomalous cross-field diffusion coefficients $D_{perp}$ of 1 $m^2/s$ and 2 $m^2/s$ exemplarily for case 1. As for the outer divertor simulations the integration time dt to calculate the test particle trajectories has been reduced by a factor of ten from 1E-9 s to 1E-10 s. Figure 22 shows the resulting profiles of the net tungsten deposition/erosion along the inner divertor target. The profiles reveal a reduced transport of sputtered ions towards the PFR if cross-field diffusion is considered. This results in lowered peaks of net deposition and towards the SOL to lowered net erosion rates. Thus, cross-field diffusion leads to a more localised transport of sputtered tungsten ions. Table 4 summarises the surface-averaged amounts of deposition and self-sputtering, both relative to the gross-erosion, the amount of prompt deposition relative to the overall deposition and the peak net erosion for the various assumptions of cross-field diffusion.

## 4.3. Main wall tiles at inner and outer midplane and outboard baffle entrance

### 4.3.1 Basic set-up for the main wall midplane tiles: simulation volume and magnetic field

Figure 23 a) shows exemplarily the poloidal cross section of the outer midplane region as contained in SOLPS. The figure also includes schematically the according ERO simulation volume, which is presented enlarged in figure 23 b), illustrating the general set-up for the ERO simulations. The x-coordinate in ERO corresponds to the toroidal direction and the z-coordinate to the direction along the major radius of STEP. The simulated wall tiles have a length of 200 mm along x- and y-direction, where the y-coordinate corresponds to the poloidal direction. The simulation volume in z-direction covers 320 mm in case of the outer midplane and 260 mm for the inner midplane simulations. For the ERO simulations of the midplane tiles two cases for the background velocity are considered as parameter study: small flow and large flow as indicated in figure 23 b) by placing the simulation volume at different distances to the stagnation point. For the "small flow" case (see also figure 23 b)) the flow velocity has values between zero at the stagnation point and $2.5 \cdot 10^{-3} \cdot c_S$ (with $c_S$ the sound speed) at a distance s = 200 mm from the stagnation point. Within the simulation volume of the "large flow" case the flow velocity is everywhere about $0.45 \cdot c_S$.
The magnetic field strength and direction are $B_{tor}$ = 1.45 T, $B_{pol}$ = -1.45 T at the outer midplane and $B_{tor}$ = 6.48 T, $B_{pol}$ = -1.28 T at the inner midplane. For the ERO simulations the magnetic field is assumed to be constant within the simulation volumes. The angle $\alpha_B$ between the magnetic field and the surface is about 1°.

### 4.3.2 Plasma parameter for the main wall midplane tiles

The electron temperature $T_e$ and density $n_e$ and the ion temperature $T_i$ based on SOLPS simulations are available as radial profiles towards the wall surface. One plasma set each for the outer and inner midplane ERO simulations is considered. Figure 24 presents the according plasma profiles along the z-coordinate as used in ERO and introduced in section 4.3.1. As the last SOLPS grid point does not reach the wall surface, an extrapolation of the plasma parameters towards the wall surface is necessary. To estimate the upper limit of tungsten erosion it is assumed that the plasma parameters stay constant when approaching the wall. The values of the plasma parameters at the wall surface thus correspond to the values from the last SOLPS grid point, which are indicated in figure 24. It is seen that the electron and ion temperatures at the inner midplane are significantly higher than at the outer one, whereas the electron density is larger at the outer midplane. The plasma parameters along the midplane surfaces (i.e. along x- and y-direction) included in the ERO simulations are constant. The radial profiles along the z-direction as shown in figure 24 are directly imported in ERO, thus without any fitting. The $Ar^+$ concentration within the plasma is set to 1% relative to the deuterium ion flux.
Table 5 summarises the plasma parameters at the outer and inner midplane surfaces together with the deuterium ion flux (according to formula (2)) and the resulting tungsten sputter yields due to $D^+$ and $Ar^+$ impact. It is clearly seen that in both cases the tungsten sputtering is dominated by the $Ar^+$ whereas deuterium ion sputtering is negligibly small even at an argon concentration of only 1%. The effect of tungsten sputtering by deuterium atoms will be discussed for the outer midplane.

### 4.3.3 Outer midplane simulations

First of all the influence of the background flow velocity is analysed. The effect of the anomalous cross-field diffusion will be studied later on and thus as a start $D_{perp}$ is set to zero. Figure 25 presents the simulated distribution of tungsten atoms and ions above the outer midplane surface considered in the ERO simulations for the "small flow" and "large flow" cases. The concentrations are integrated along the poloidal (y-direction). The difference in these distributions for small and large flow is not very pronounced. However, viewing the distribution of ions from top, i.e. along the radial direction, reveals the effect of the flow velocity as shown in figure 26 for $W^{3+}$ ions. With the large background flow the ions are driven along the flow (the flow is assumed to be parallel to the B-field, see figure 23 b)) leading to larger concentrations in plus x- and minus y-direction. In the case of small (negligible) flow the W ion transport is dominated by the gyration along the B-field without preferred transport parallel or anti-parallel to the B-field. The different transport is also evident in the different numbers of tungsten particles lost from the simulation volume. The large flow leads to increased losses towards plus x- and minus y-direction, whereas for the small flow case the losses are similar in these directions. The overall particle loss is comparable for the small and large flow case (about 75%).
The tungsten gross erosion, self-sputtering and deposition along the outer midplane tile is shown in figure 27 for the small and large flow condition. The gross erosion caused by the background plasma leads to homogeneous erosion pattern as the plasma parameters are constant along the surface. The visible structure is due to self-sputtering of eroded tungsten ions returning to the surface. The gross erosion rates (averaged over the surface) and percentage amounts of deposition, prompt deposition and self-sputtering are summarised in table 6. The percent numbers are given relative to the amount of gross erosion. The numbers for the large flow case are very similar to the ones of the small flow simulation. In particular it is seen that, as expected, also the amount of prompt deposition is independent of the flow assumption. The overall deposition in both cases is

strongly dominated by prompt deposition. Eroded tungsten, which reaches a certain distance from the surface cannot be locally deposited as it mainly flows along the magnetic field, which is almost parallel to the surface, and thus finally leaves the simulation volume. The assumption of the background flow therefore has almost no impact on the local deposition. However, depending on the strength and direction, it will influence the global transport of tungsten particles, which are not locally deposited and therefore the flow also will influence the global deposition pattern. The amount of tungsten self-sputtering is very small and below 0.1%. This is a consequence of the rather small plasma temperature leading to small electric sheath and hence returning tungsten ions cannot gain sufficient energy for significant sputtering.
To study the influence of anomalous cross-field diffusion, additional simulations with $D_{perp}$ = 1 $m^2/s$ and 2 $m^2/s$ have been carried out. As the previous simulations have shown the negligible effect of the background flow velocity on the local transport of eroded tungsten, in the following only the results for the small flow case are presented. The amounts of deposition and prompt deposition increase with increasing cross-field diffusion reaching nearly 60% deposition for $D_{perp}$ = 2 $m^2/s$, see table 6. Also, with perpendicular cross-field diffusion there is now a certain amount of tungsten that is non-promptly deposited. As for the case without perpendicular diffusion the self-sputtering with cross-field diffusion is negligibly small due to the low plasma temperature.

**Effect of tungsten sputtering by neutral deuterium atoms:**
The energy distributions of neutral deuterium atoms hitting the outer midplane has been made available for five different plasma cases as result from of SOLPS simulations equipped with a dedicated "diagnostic surface" located at the outer midplane to collect the impact energies of deuterium atoms hitting that area. It is seen that only a rather small amount of the neutral deuterium atoms (between 10% and 16%) has energies larger of 250 eV, the threshold energy of tungsten sputtering by deuterium atoms.
To estimate the tungsten sputtering caused by neutral deuterium atoms the according sputtering yields in dependence on the impact energy and angle are needed. As the angular distribution is not available a fixed impact angle is assumed. Instead of applying the Eckstein fit formula to calculate the sputtering yields dependent on the energy and angle (as it is done inside the ERO code for traced particles) here, for convenience, pre-calculated data according to SDTrimSP calculations by W. Eckstein [35] are applied. The sputtering yields shown in figure 1 cannot be used here as they are given as function of the electron and ion temperature since they are intended to be used for Maxwellian distributed background ion species considering the sheath potential. For the following gross erosion estimations the energy-dependent data corresponding to an impact angle of 65° are applied. Depending on the impact energy, the sputtering yields at that angle are at or near to the maximum. Therefore the overall erosion flux serves as an upper limit. The according resulting tungsten erosion fluxes for the five cases range between 7E15 and 3E16 W /$m^2/s$. These fluxes can be compared with the tungsten gross erosion of 1.3E17 W /$m^2/s$ caused by plasma impact at the outer midplane (or more precisely argon ion impact as the energy of deuterium ions is too low for significant tungsten sputtering). It is seen that sputtering due to deuterium atoms is at least a factor of about 4 smaller than sputtering due to argon ions from plasma impact.

### 4.3.4 Inner midplane simulations

As for the outer midplane, simulations have been done for the inner midplane without cross-field diffusion and with perpendicular diffusion applying $D_{perp}$ = 1 $m^2/s$ and 2 $m^2/s$. Small and large background flow has been applied, showing again no significant difference in the resulting local erosion and deposition. Figure 28 illustrates (for the small flow assumption) the resulting tungsten

atoms and ions distribution for the case without cross-field diffusion and as example with $D_{perp}$ = 2 $m^2$/s. As typically observed, cross-field diffusion results in disturbed ion trajectories and one can expect increased deposition. This indeed is the case as can be seen from the amounts of deposition summarised in table 6, which also includes the corresponding information from the outer midplane simulations for comparison.
Table 6 reveals that the gross erosion at the inner midplane is about 10 times larger than at the outer one. This is a consequence of higher electron and ion temperatures at the inner midplane. As for the outer midplane also for the inner midplane tile the overall deposition is dominated by prompt deposition if no cross-field diffusion is included in the simulations. At the inner midplane the amount of prompt deposition without cross-field diffusion is a factor of about two smaller than at the outer one. This can be explained with the larger magnetic field resulting in smaller gyration radius and thus smaller prompt deposition. Considering cross-field diffusion leads also for the inner midplane to larger deposition (and also prompt deposition) - the overall deposition is similar for inner and outer midplane reaching values of 50 - 60% with cross-field diffusion. All cases show very small amounts of self-sputtering. Due to the larger plasma temperature, self-sputtering is about 10 times larger at the inner compared to the outer midplane, but still below 1% for all cases studied.

### 4.3.5 Outboard baffle entrance

Simplified studies of gross erosion estimates as supplement to the previous ERO erosion/deposition simulations are carried out to provide information about one additional area within the main wall, which could suffer from significant erosion. Figure 29 shows a poloidal cross section of the SOLPS grid and the wall geometry around the outboard baffle entrance. Indicated in light blue are 11 grid points from which the plasma parameters are used for the erosion estimations. To get an upper limit of the erosion no fitting is done between the grid points and the actual wall location, but instead the plasma parameters at these grid points are employed to calculate the erosion rates. Figure 30 summarises the according electron and ion temperature and the electron density of the 11 grid points under consideration from a typical SOLPS simulation.
It is seen that the electron temperature ranges between 1 and 4 eV, the ratio of $T_i/T_e$ is between 1 and 1.25. According to figure 1 it follows that at these temperatures tungsten sputtering due to deuterium ions is negligible. The sputtering due to argon ions ($Ar^+$) is rather small with yields not larger than 4E-5. The plasma parameters, deuterium ion flux and the tungsten sputtering yields and resulting gross erosion fluxes are summarised in table 7. The deuterium ion flux has been calculated assuming a magnetic field angle of 1° relative to the surface. Figure 31 presents the estimated gross erosion fluxes at the outboard baffle entrance in comparison with the tungsten gross erosion fluxes calculated with ERO at the outer and inner divertor and at the outer and inner midplane. It can be concluded that the tungsten gross erosion fluxes at the outboard baffle entrance are small compared to the gross erosion at the inner and outer divertor and also at the inner and outer midplanes. However, one has to keep in mind that the fraction of deposition of eroded tungsten, in particular within the divertor, can be rather high with values even larger than 98% depending on the plasma conditions. The tungsten deposition fraction at the baffle entrance is probably much smaller (and could be comparable with the deposition fractions at the midplanes, which have been estimated to 10 - 60% depending on the assumption for the cross field diffusion). Thus the difference of the net tungsten erosion flux between the divertor and the baffle entrance can be significantly smaller than the difference seen in the gross erosion.

## 5. Conclusions and outlook

ERO simulations for STEP have been done for the outer and inner divertor, the outer and inner midplane and the entrance region of the outboard baffle to estimate the tungsten erosion and deposition for steady state plasma conditions. The plasma parameters have been provided by SOLPS simulations performed with argon puffing for plasma edge cooling.

The main results can be summarised as following:

***Outer divertor:***

- For the five different plasma conditions studied, tungsten erosion is dominated by argon whereas the energy of the deuterium ions is below or very near to the tungsten sputtering threshold. The simulated tungsten gross erosion strongly depends on the plasma parameters and the argon concentration in the plasma. For the cases studied, the peak gross erosion ranges from 5E16 to 6.7E19 W atoms /$m^2$/s. The comparably low minimum gross erosion is a consequence of the very small argon concentration in the plasma for that specific case.
- The modelled amount of tungsten deposition is large for the studied cases with surface-averaged values between 83% and 98%, relative to the gross erosion. Higher electron temperatures, ion temperatures and electron densities lead to larger amounts of deposition. Self-sputtering of tungsten by returning tungsten ions is between 26% and 46% relative to the overall gross-erosion and reveals a similar dependence on the plasma parameters as the amount of deposition. The magnetic field geometry leads to transport of sputtered tungsten towards the SOL due to friction with the background plasma resulting in net erosion around the strike point and a region of net deposition within the SOL. The simulated net peak erosion ranges from 5E-4 to 0.3 nm/s.
- For two selected cases parameter variations have been studied. It has been seen that the reversal of the magnetic field direction can influence the transport of sputtered tungsten due to reversal of the E×B drift and also the gyration direction of tungsten ions. For the considered cases, the reversed B field leads to an increased transport towards the PFR, which can reduce the net erosion peak (for the studied cases a reduction of up to about 30%). The influence of an anomalous cross-field diffusion has been studied showing that its consideration leads to more localised deposition and thus reduction of the peak net erosion by up to about 60% with a diffusion coefficient of 2 $m^2$/s compared to the simulation without cross-field diffusion.

***Inner divertor:***

- Three different plasma conditions have been studied. For the given plasma conditions, tungsten erosion is dominated by argon whereas the energy of the deuterium ions is below or near to the tungsten sputtering threshold. The simulated tungsten gross erosion strongly depends on the plasma parameters and the argon concentration in the plasma. For the cases studied, the peak gross erosion ranges from 1.4E16 to 1.1E19 W atoms /$m^2$/s. The comparably low minimum gross erosion is a consequence of the smallest electron and ion temperatures and also smallest electron densities for that specific case.
- The modelled amount of tungsten deposition is large for the studied cases with surface-averaged values between ~88% and ~99%, relative to the gross erosion. Higher electron temperatures, ion temperatures and electron densities lead to larger amounts of deposition. Self-sputtering of tungsten by returning tungsten ions is between 5% and 30% relative to the overall gross-erosion and reveals a similar dependence on the plasma parameters as the amount of deposition. The magnetic field geometry leads to transport of sputtered tungsten towards the

PFR due to friction with the background plasma resulting in net erosion areas in the SOL and a region of net deposition towards the PFR in the vicinity of the gross erosion peak. The simulated net peak erosion ranges from 1E-4 to 0.04 nm/s.

- For one case parameter variations have been studied. It has been seen that the reversal of the magnetic field direction can influence the transport of sputtered tungsten due to reversal of the E×B drift and also the gyration direction of tungsten ions. For the considered case, the reversed B field leads to an increased transport towards the SOL, which reduces the net deposition peak and at the same time lowers the net erosion rates. The influence of anomalous cross-field diffusion has been analysed showing that its consideration leads to more localised deposition and thus reduction of the peak net erosion by up to about 30% with a diffusion coefficient of 2 $m^2/s$ compared to the simulation without cross-field diffusion.

***Midplane wall tiles:***

- For the plasma parameters studied, tungsten sputtering by D ions is negligible. First estimations for the outer midplane indicate that the tungsten erosion due to deuterium atoms is at least four times smaller than the erosion due to the argon ions.
- The local deposition of eroded tungsten ranges between 12% (inner midplane without cross-field diffusion) and 60% (inner and outer midplane with cross-field diffusion of 2 $m^2/s$) and is dominated by prompt deposition if cross-field diffusion is not included in the simulations. Cross-field diffusion increases the deposition, with $D_{perp}$ = 2 $m^2/s$ by more than a factor of two for the outer and a factor of about 5 for the inner midplane.
- The assumptions for the background flow velocity do not significantly influence the local deposition but can have an effect on the global transport of eroded tungsten, which is not locally deposited.
- The erosion rates at the inner midplane are a factor of about 15 larger than at the outer midplane. The gross erosion is about 1.9E18 W atoms /$m^2$/s for the inner and 1.3E17 W atoms /$m^2$/s for the outer midplane. The net erosion ranges from 1E-3 nm/s to 1.6E-3 nm/s for the outer and from 1.3E-3 nm/s to 2.9E-2 nm/s for the inner midplane, depending on the assumption for the anomalous cross-field diffusion.

***Outboard baffle entrance:***

- With the plasma parameters studied it is seen that the erosion is solely due to argon ions whereas the impact energy of deuterium ions is below the threshold for tungsten sputtering. Sputtering by deuterium atoms has not been considered.
- The resulting tungsten gross erosion fluxes assuming 1% $Ar^+$ are clearly lower (at least a factor of 35) than the modelled gross erosion fluxes at the outer midplane, and the inner and outer divertor. However, the difference in the net erosion fluxes, which also consider the deposition of eroded tungsten, can be smaller as in particular the fraction of deposition within the divertor is expected to be significantly higher than at the baffle entrance.

Taking from all simulations the largest modelled net erosion rate of 0.3 nm/s (occuring at the outer divertor target) would result in about 9.5 mm/year with 24/7 operation. For comparison, the smallest net erosion in the divertor within the parameter range studied is about 0.02 mm/year for the outer and about 0.002 mm/year for the inner divertor. These rates can be used to estimate limits of the target lifetime under steady state operation. Also, the simulations can provide information of the number of net eroded tungsten atoms, which for instance can be used to assess tungsten dust formation. Taking the most pessimistic cases with the highest rates results in surface-integrated

(integrated along the target in poloidal direction) net rates of 1.6E25 W/m/year for the outer and 3E24 W/m/year for the inner divertor.

In the future, the erosion due to transient events in addition to the studied steady state plasma conditions could be of interest. Moreover, the effect of surface morphology and roughness could be studied, including their dynamics as consequence of plasma exposure. In this context, also the possibly enhanced erosion of deposits compared to bulk material may play a role. The erosion of liquid surface components can be analysed. The analysis of additional magnetic field configurations and/or divertor geometries could be addressed. The simulations presented in the current work made use of a magnetic field having an angle of a few degree relative to the surface. A significant reduction of that angle would decrease the plasma flux to the surface and as consequence also the gross erosion. Finally, ERO2.0 [36, 37] modelling could be performed for global simulations of the whole STEP device providing a more self-consistent picture of tungsten erosion, migration and deposition. This for instance would also provide information of tungsten transport from the main chamber towards the divertor and vice versa. Moreover, instead of constant argon concentration and charge state in the background plasma assumed within the present work, ERO2.0 could use spatially varying concentrations and charge states for the impinging argon to further improve the gross erosion estimates.

## 6. Acknowledgements

This work has been carried out within the framework of an UKAEA service contract with the reference T/LD065/21.

## References


[1] H. Wilson, I. Chapman, T. Denton, W. Morris, B. Patel, G. Voss, C. Waldon, the STEP Team (2020), *STEP—on the pathway to fusion commercialization*, Commercialising Fusion Energy, IOP Publishing, doi:10.1088/978-0-7503-2719-0ch8
[2] A. Kirschner et al., Nucl. Fusion 40 (2000) 989
[3] A.S. Kukushkin et al., Fusion Eng. Des. 86 (2011) 2865
[4] R.T. Osawa et al., Nucl. Fusion 63 (2023) 076032
[5] W. Eckstein et al., *SDTrimSP: A Monte-Carlo code for calculating collision phenomena in randomized targets*, Report IPP 12/3 (2007)
[6] K. Schmid et al., Nucl. Fusion 50 (2010) 105004
[7] D. Borodin et al., Phys. Scr. T159 (2010) 014057
[8] L.A. Vainstein et al., J. Phys. B: At. Mol. Opt. Phys. 44 (2011) 125201
[9] P. Stangeby, *The plasma boundary of magnetic fusion devices*, Institute of Physics Publishing, Bristol and Philadelphia (2000)
[10] A. Kirschner et al., Plasma Phys. Control. Fusion 60 (2018) 014041
[11] W. Eckstein, *Computer simulation of ion-solid interactions, Springer*, Berlin (1991)
[12] W. Eckstein, Vacuum 82 (2008) 930
[13] A. Kirschner et al., Phys. Scr. T91 (2001) 57
[14] S. Droste et al., Plasma Phys. Control. Fusion 50 (2008) 015006
[15] R. Ding et al., Plasma Phys. Control. Fusion 52 (2010) 045005
[16] A. Kirschner et al., J. Nucl. Mat. 438 (2013) S723
[17] A. Kirschner et al., Nucl. Mat. Energy 12 (2017) 564
[18] D. Borodin et al., J. Nucl. Mat. 438 (2013) S267
[19] A. Kirschner et al., J. Nucl. Mat. 463 (2015) 116
[20] D. Borodin et al., Nucl. Mat. Energy 9 (2016) 604
[21] A. Kirschner et al., Nucl. Mat. Energy 18 (2019) 239
[22] L. Aho-Mantila et al., Contr. Plasma Phys. 50, No. 3-5 (2010) 439
[23] L. Aho-Mantila et al., Nucl. Fusion 52 (2012) 103007
[24] R. Ding et al., Nucl. Fusion 55 (2015) 023013
[25] Shuyu Dai et al., Nucl. Fusion 55 (2015) 043003
[26] H. Xie et al., Phys. Plasmas 24 (2017) 092512
[27] G. Kawamura et al., Contrib. Plasma Phys. 50, No. 3-5 (2010) 451
[28] G. van Swaaij et al., Plasma Phys. Control. Fusion 56, Issue 9 (2014) 095028
[29] D. Borodin et al., Nucl. Mat. Energy 12 (2017) 1157
[30] S. Brezinsek et al., Nucl. Fusion 59 (2019) 096035
[31] A. Kirschner et al., J. Nucl. Mat. 363-365 (2007) 91
[32] A. Kirschner et al., J. Nucl. Mat. 390 (2009) 152
[33] A. Kirschner et al., Phys. Scr. T138 (2009) 014011
[34] D. Borodin et al., Phys. Scr. T145 (2011) 014008
[35] W. Eckstein, *Calculated Sputtering, Reflection and Range Values*, Report IPP 9/132, June 2002
[36] J. Romazanov et al., Phys. Scr. T170 (2017) 014018
[37] J. Romazanov et al., Nucl. Fusion 62 (2022) 036011

## Figures

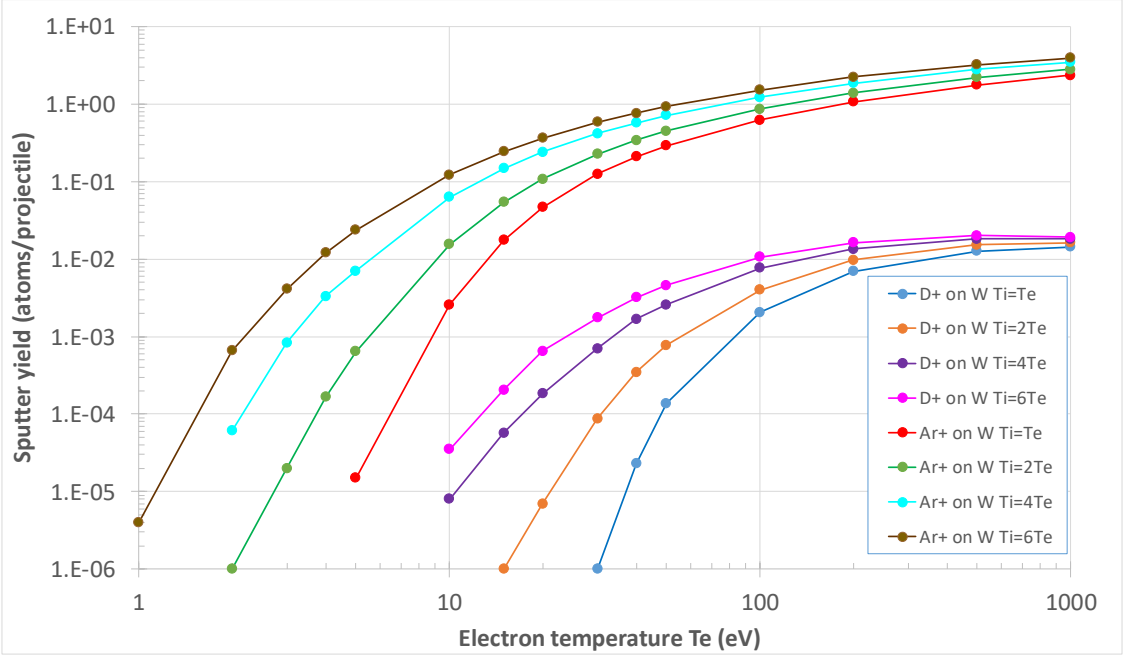


***Figure 1*** *Tungsten sputter yields for deuterium $D^+$ and argon $Ar^+$ ions calculated with SDTrimSP for 60° impact and Maxwellian-distributed projectiles. A sheath potential of $3T_e$ is considered. The yields are provided as function of $T_e$ for different ratios of $T_i/T_e$ = 1, 2, 4 and 6.*

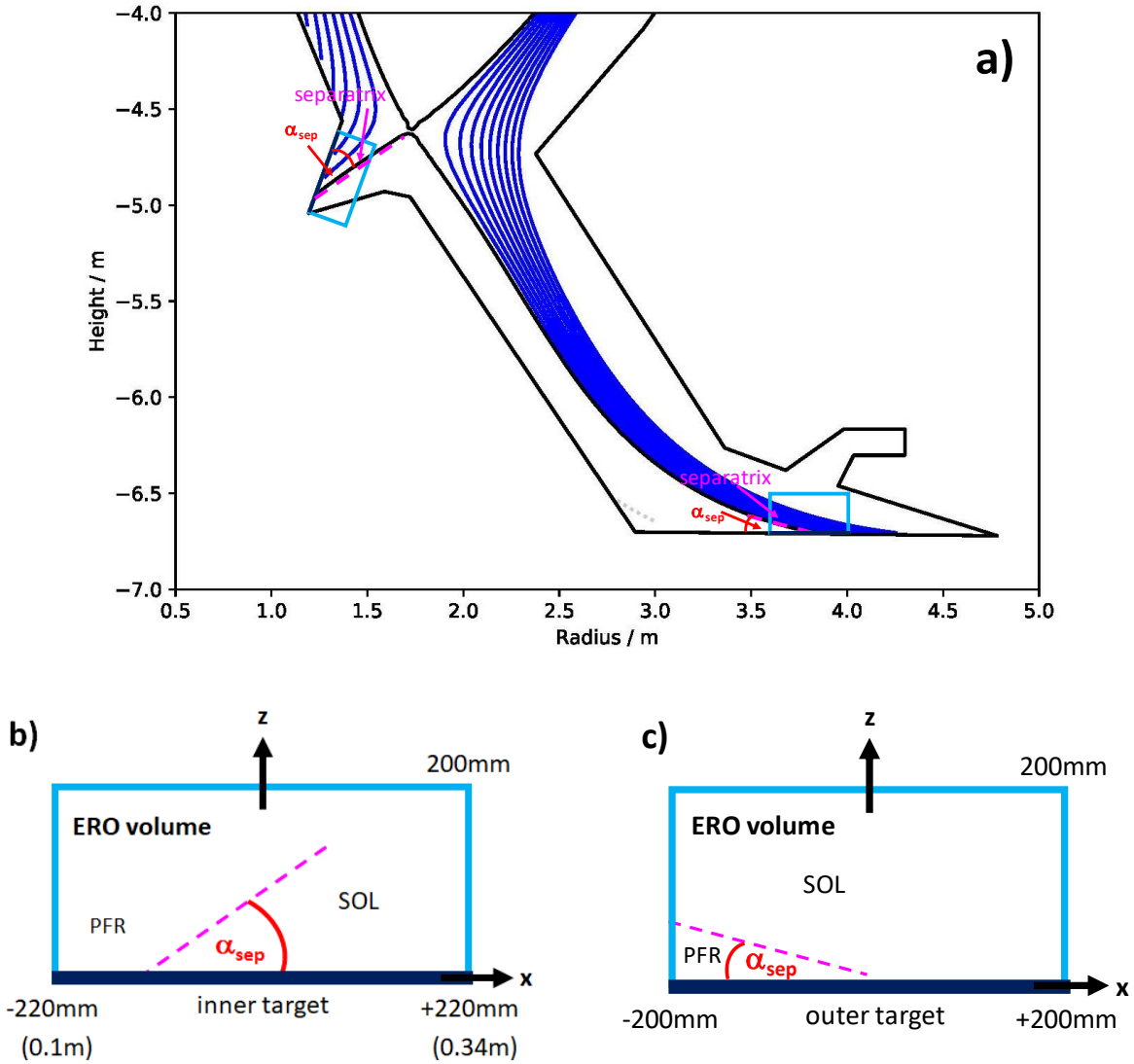


***Figure 2 a)*** *Poloidal cross section of the lower divertor of STEP with the ERO simulation volumes for inner and outer lower divertor marked in blue. The blue lines represent the magnetic flux surfaces.* ***b)*** *Enlarged view of the local ERO simulation volume for the inner divertor target (after rotating by 70° clockwise and mirroring at the target plane).* ***c)*** *Enlarged view of the local ERO simulation volume for the outer divertor target.*

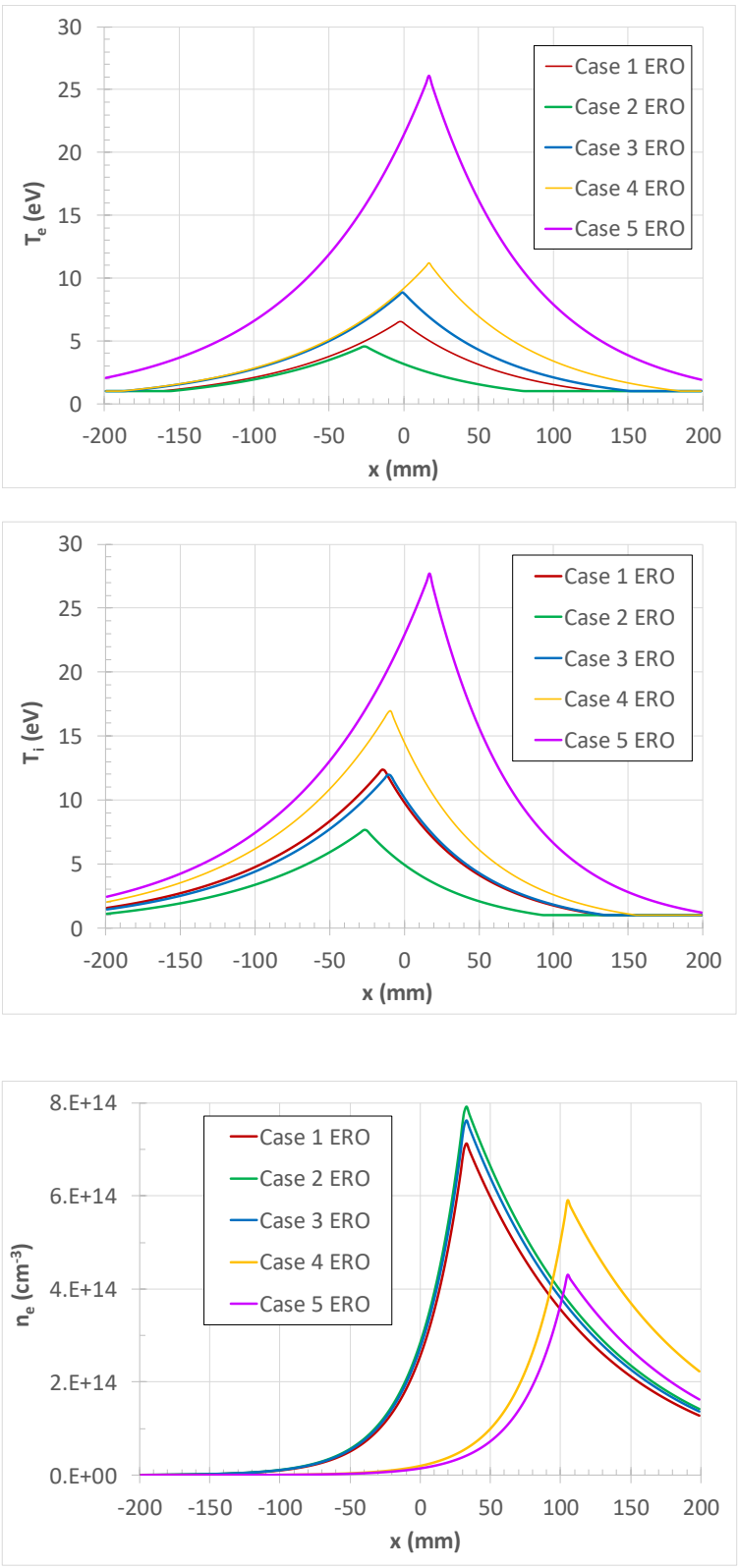


***Figure 3*** *Exponential fits of the profiles of electron temperature, ion temperature and electron density along the outer divertor target.*

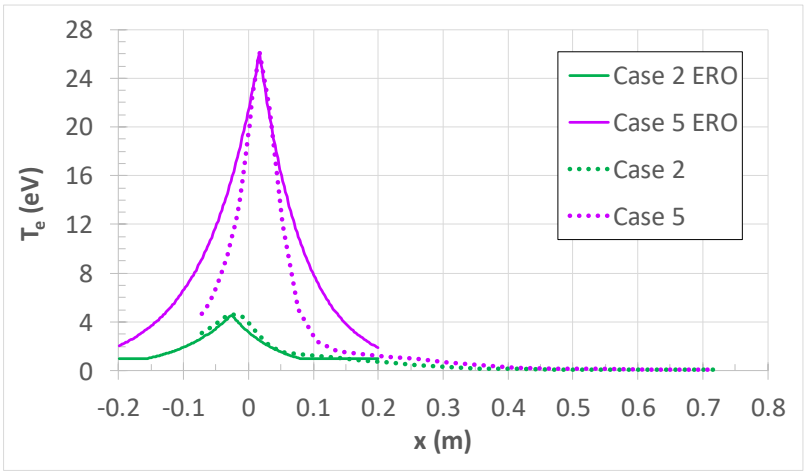


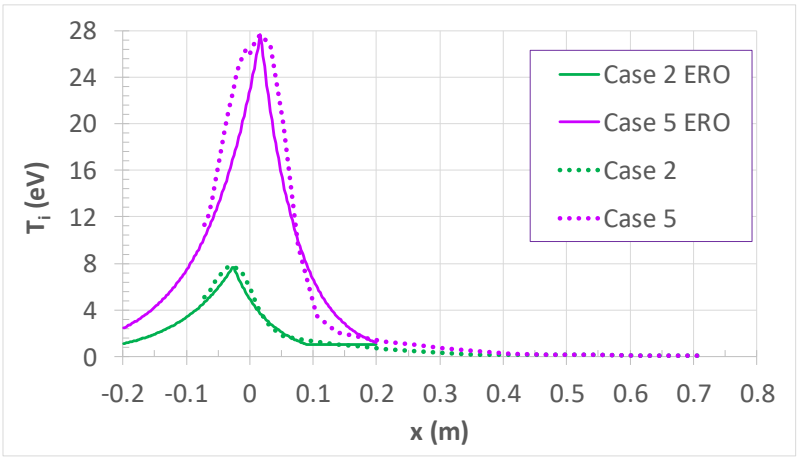


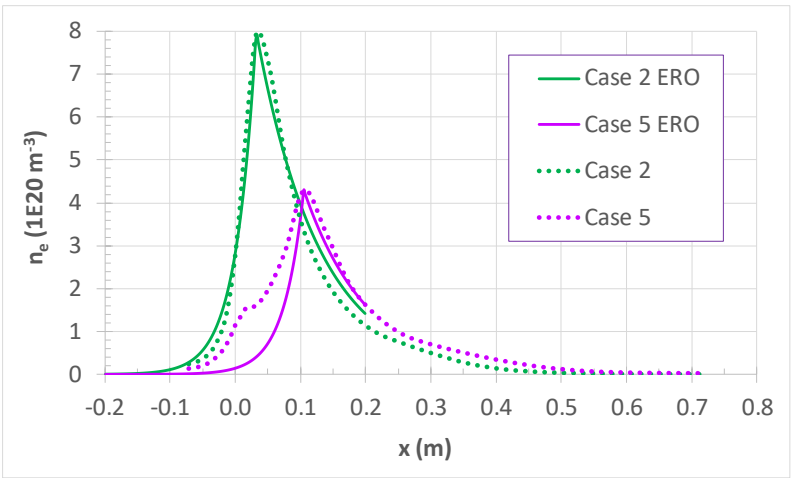


***Figure 4*** *Outer divertor target profiles of electron temperature, ion temperature and electron density for case 2 and case 5: comparison of exponential fits (solid curves marked with "ERO") and original SOLPS data (dotted curves).*

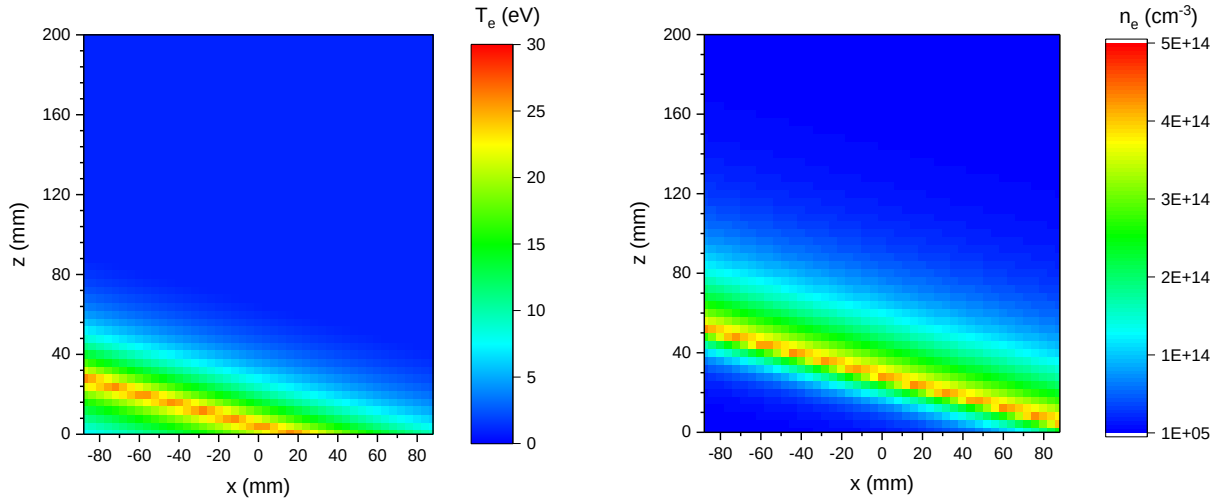


***Figure 5*** *2D distribution of electron temperature and density for the outer divertor target region for case 5. Please note that the x-axis only covers part of the overall simulated length of 400 mm.*

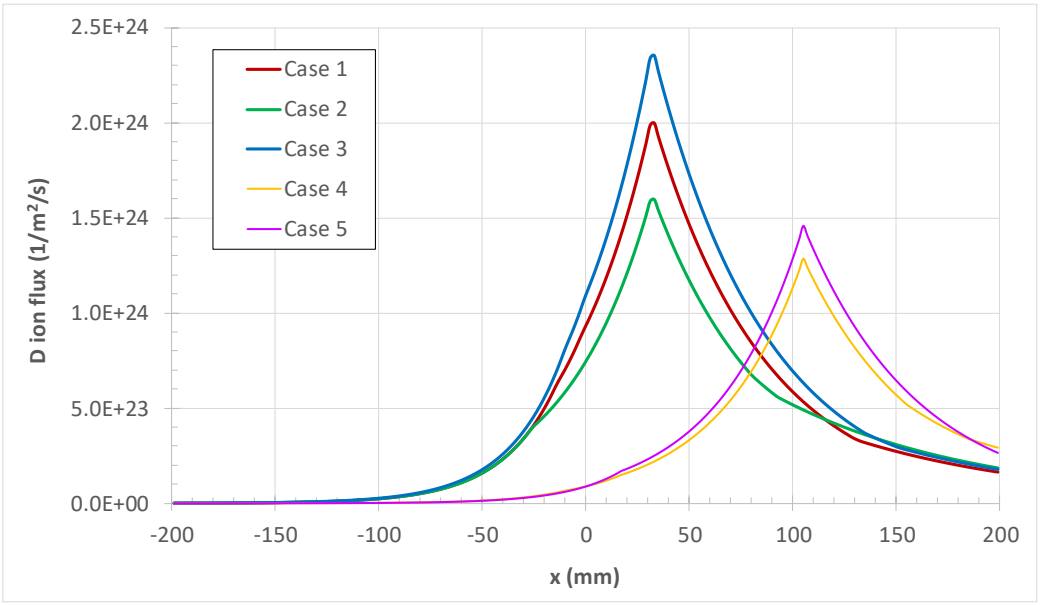


***Figure 6*** *Deuterium ion flux along the outer divertor target for the five different cases.*

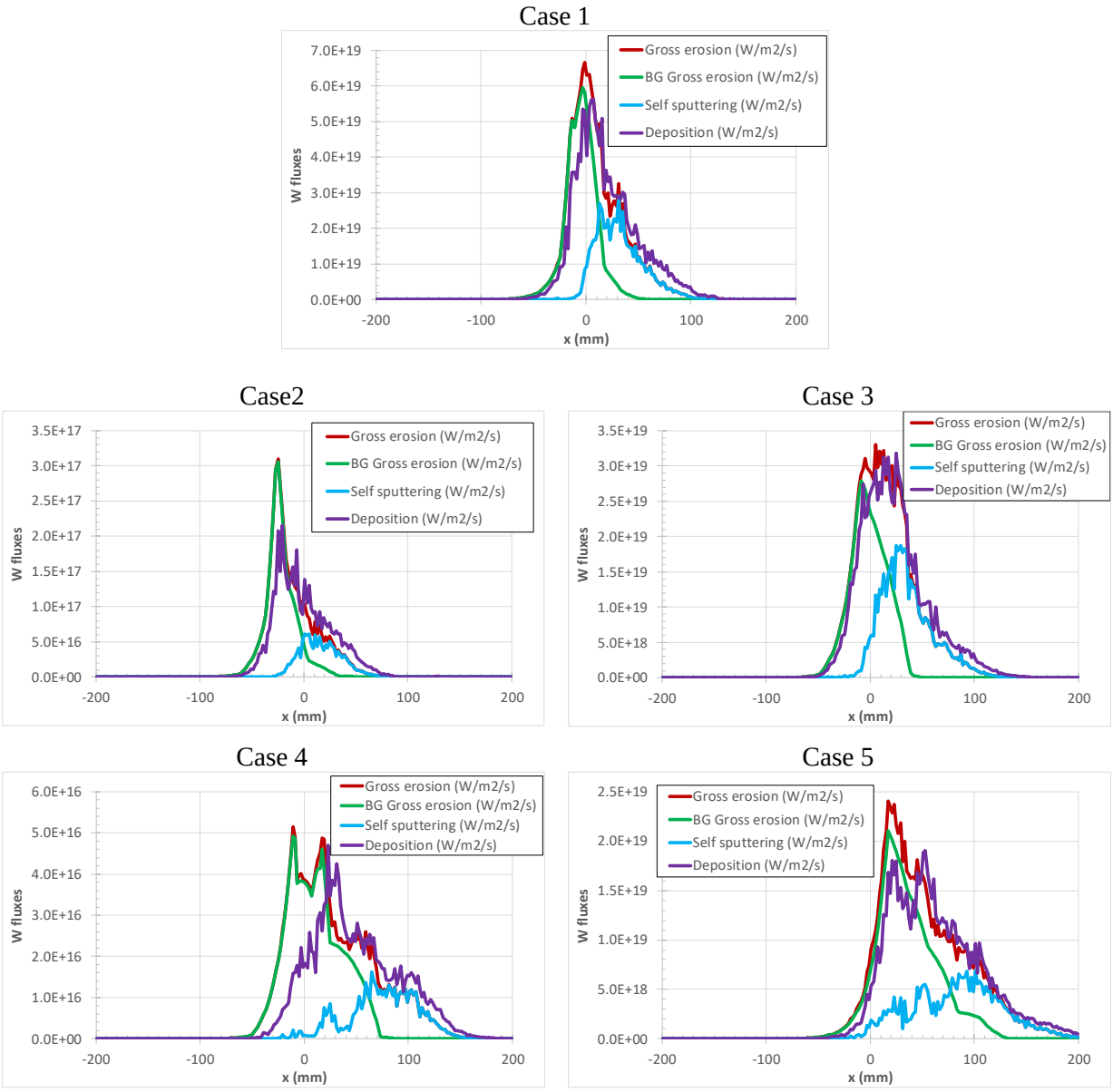


***Figure 7*** *Profiles of tungsten gross erosion, erosion by plasma background (BG) ions, self-sputtering and deposition along the outer divertor target for the five cases. Notice the different scales of the y-axes.*

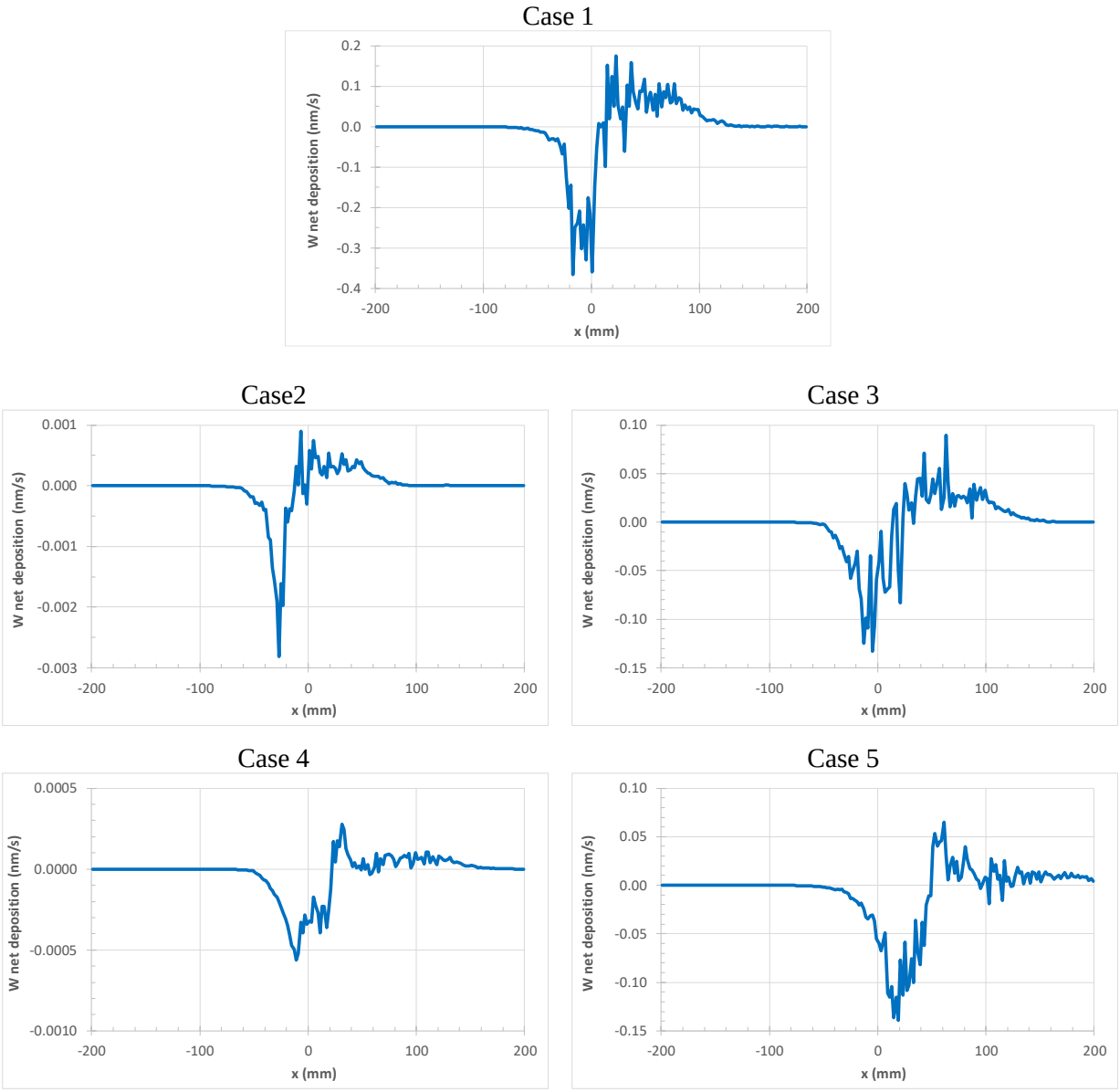


***Figure 8*** *Profiles of net tungsten deposition/erosion along the outer divertor target for the five simulation cases. Notice the different scales of the y-axes.*

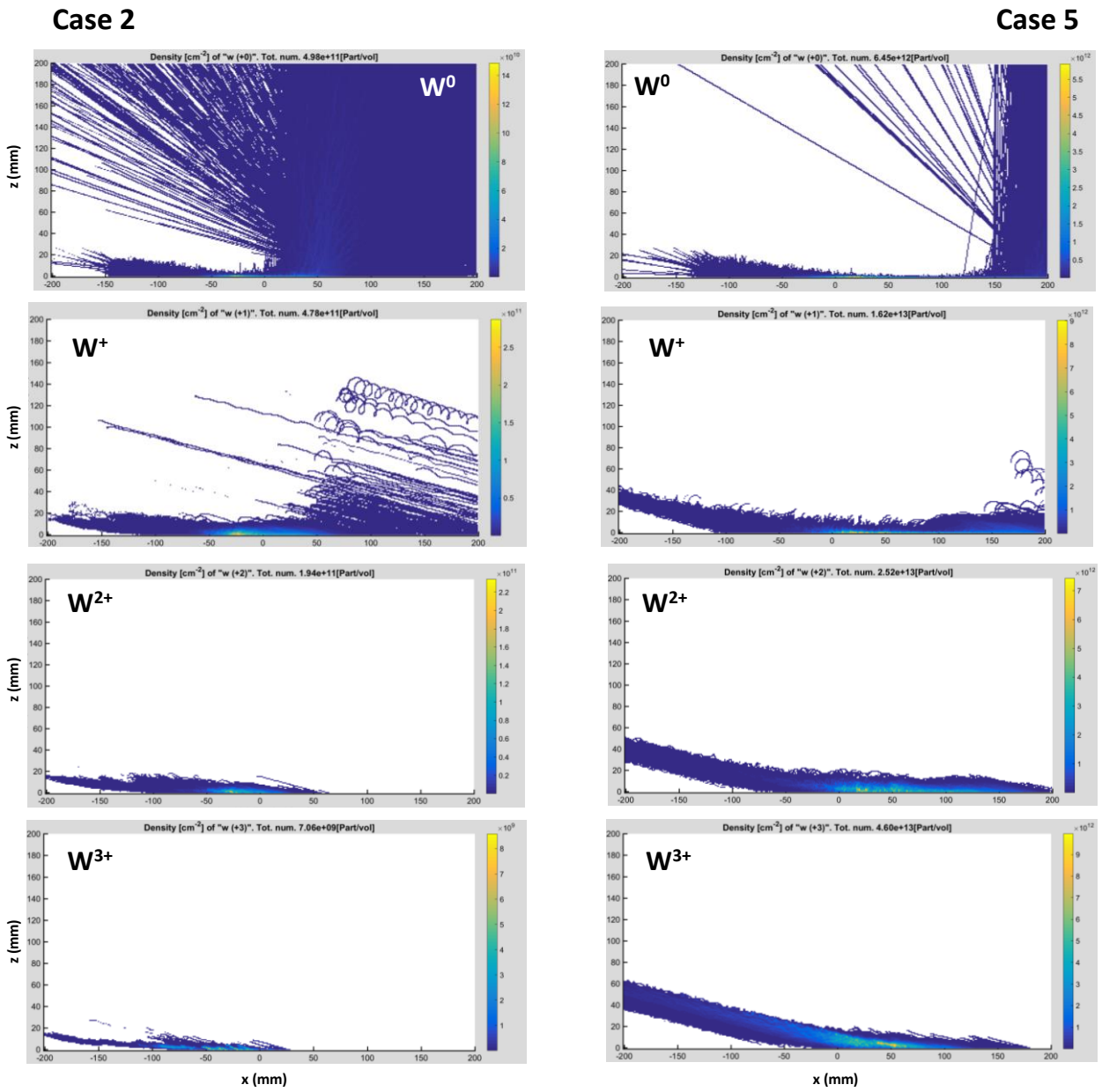


***Figure 9*** *2D distribution of tungsten atoms and charged ions above the outer divertor target for case 2 and case 5. The colour bars are in arbitrary units.*

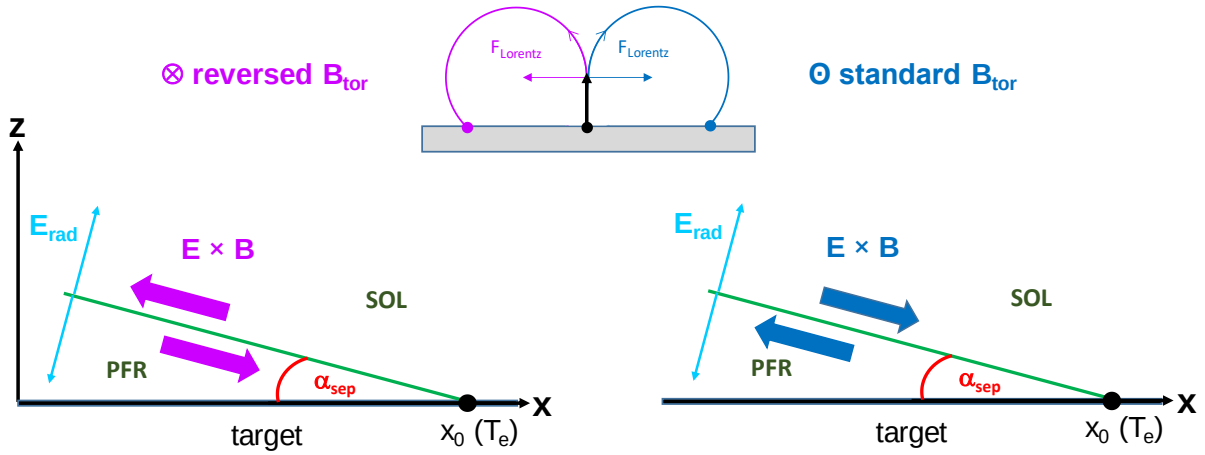


***Figure 10*** *E×B drift direction caused by the radial electric field $E_{rad}$ within the SOL and PFR of the outer divertor for reversed and standard magnetic field direction. On top of the figure the direction of the ion gyration is shown for both cases.*

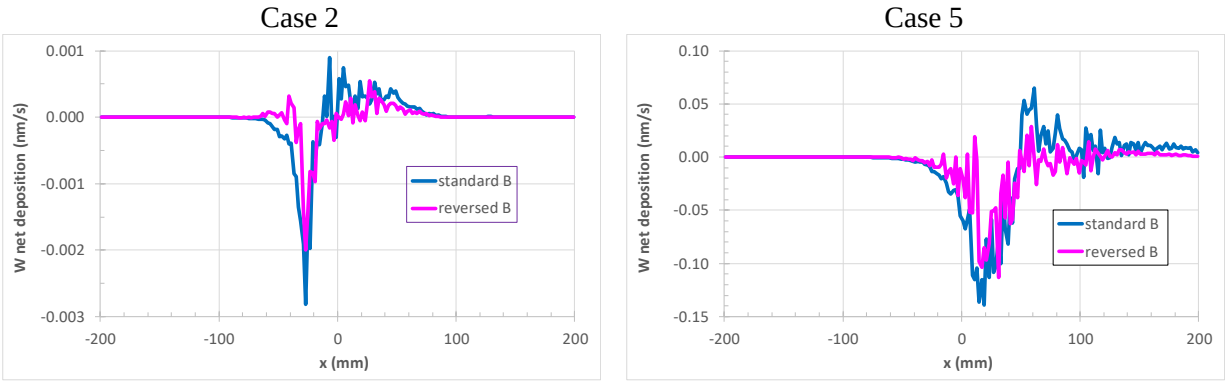


***Figure 11*** *Profiles of net tungsten deposition/erosion along the outer divertor target for case 2 and 5 without anomalous cross-field diffusion: standard B versus reversed B field direction.*

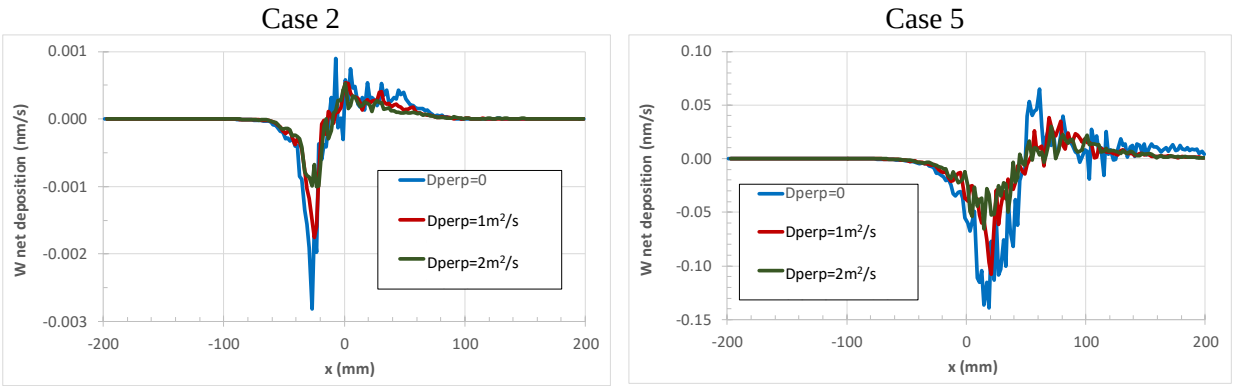


***Figure 12*** *Profiles of net tungsten deposition/erosion along the outer divertor target for case 2 and 5 with standard B field direction: study of the anomalous cross-field diffusion coefficient* $D_{perp}$*. Remark: for the profiles from the simulations with non-zero diffusion smoothing with 2 periods moving average has been applied.*

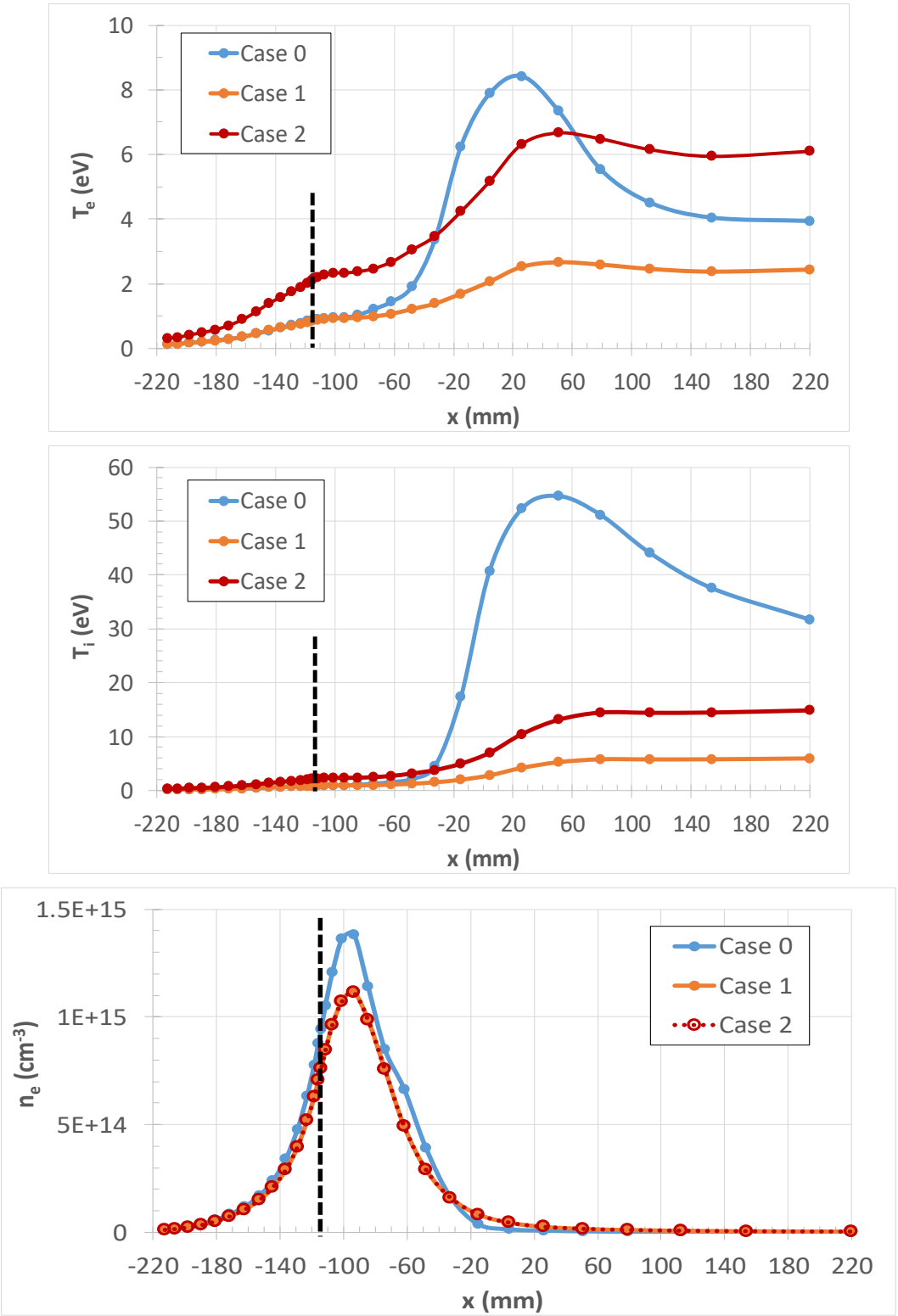


***Figure 13*** *Profiles of plasma parameter along the inner divertor target. The dashed lines indicate the ERO coordinate x = -115 mm corresponding to x = 0 mm from the SOLPS profiles´coordinates.*

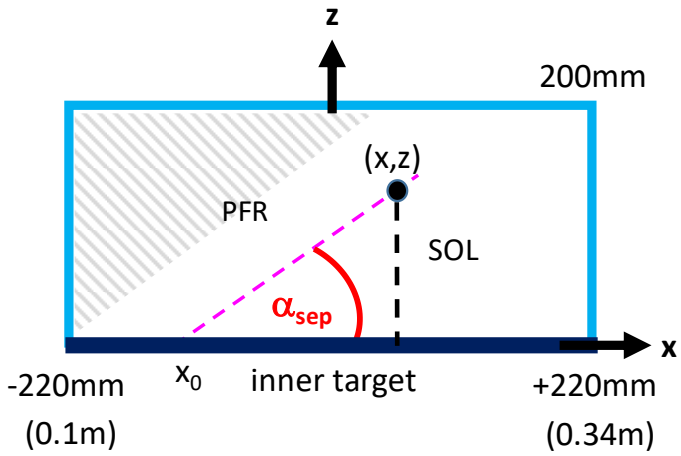


***Figure 14*** *Generation of 2D plasma via projection of e.g. position (x,z) towards the inner target along the flux surfaces to position $x_0$. Within the shaded area exponential fits are applied.*

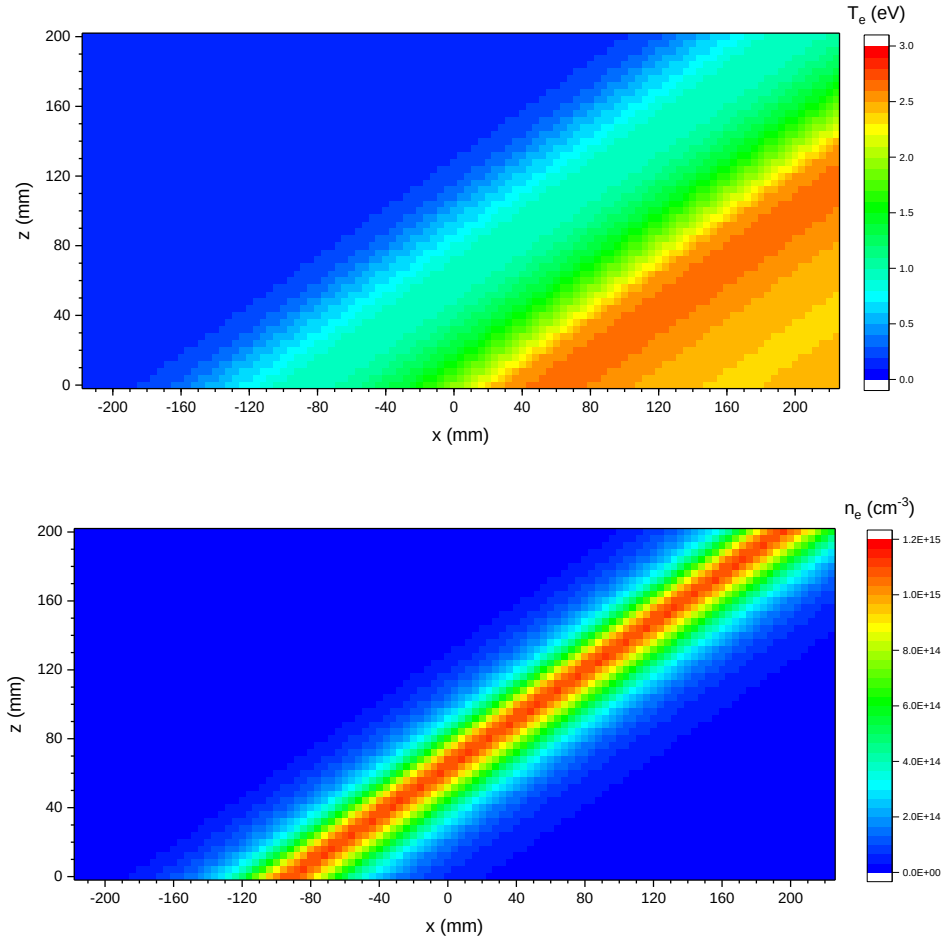


***Figure 15*** *2D distribution of electron temperature and density for case 1 within the (x,z)-plane of the inner divertor simulation volume.*

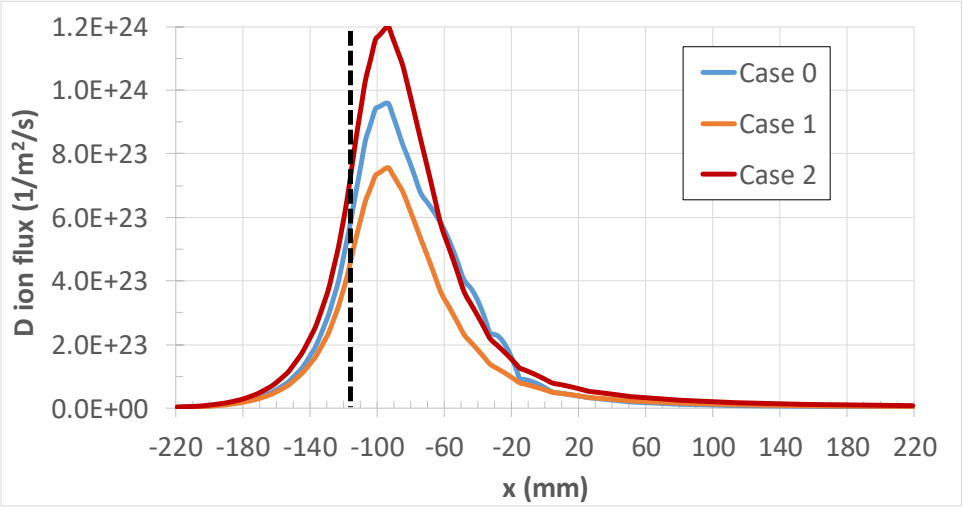


***Figure 16*** *Deuterium ion flux along the inner divertor target for the different cases.*

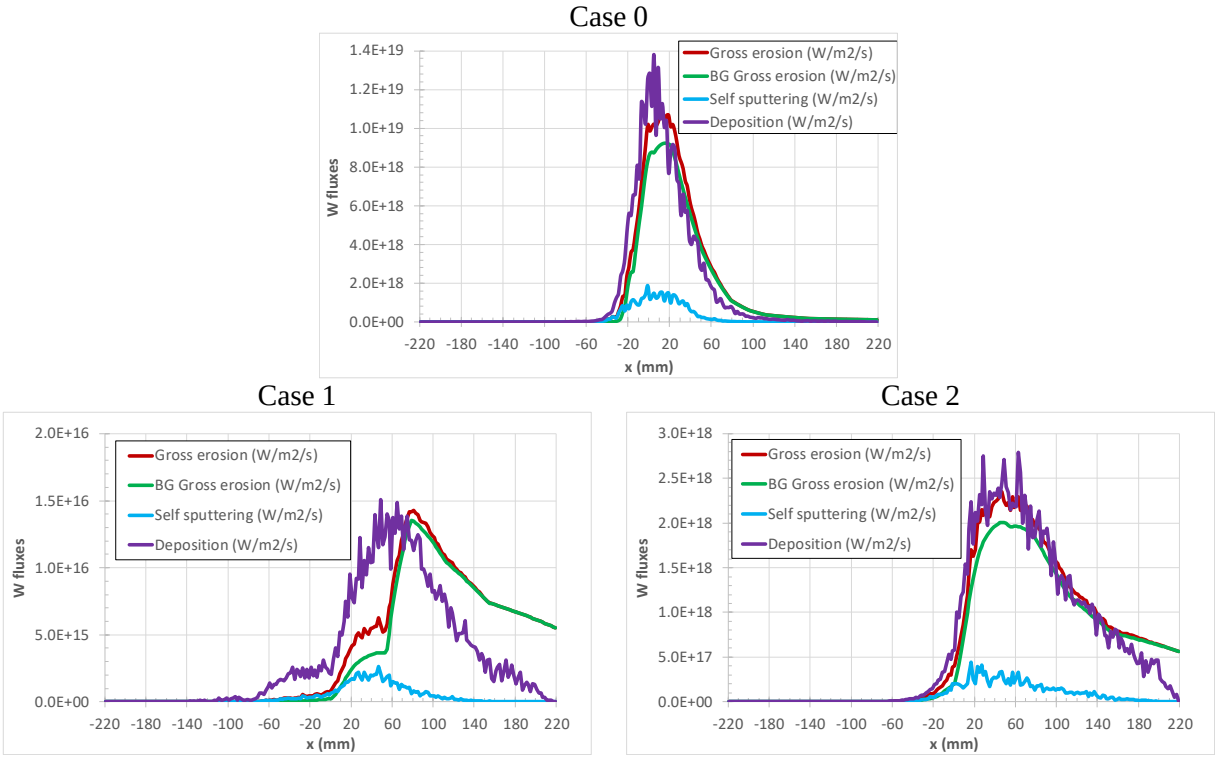


***Figure 17*** *Profiles of tungsten gross erosion, erosion by plasma background (BG) ions, self-sputtering and deposition along the inner divertor target for the 3 cases. Notice the different scales of the y-axes.*

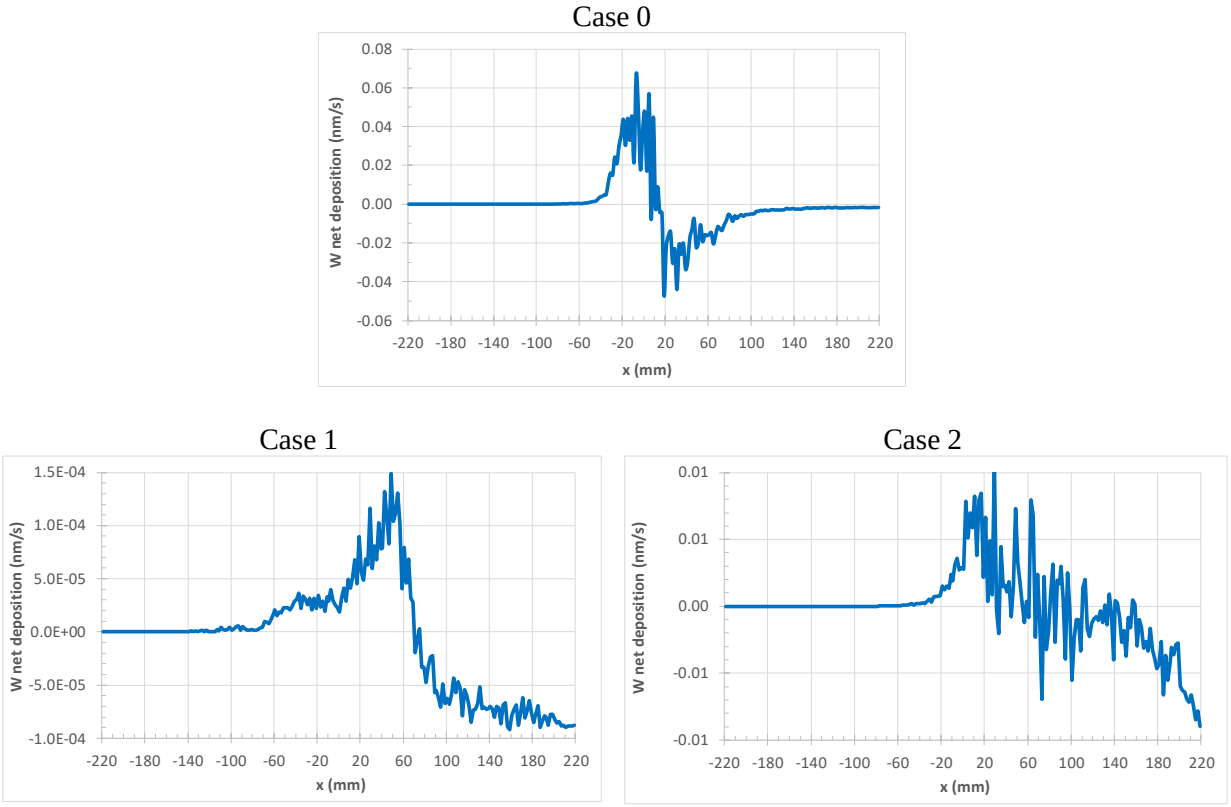


***Figure 18*** *Profiles of net tungsten deposition/erosion from the 3 simulation cases for the inner divertor target. Notice the different scales of the y-axes.*

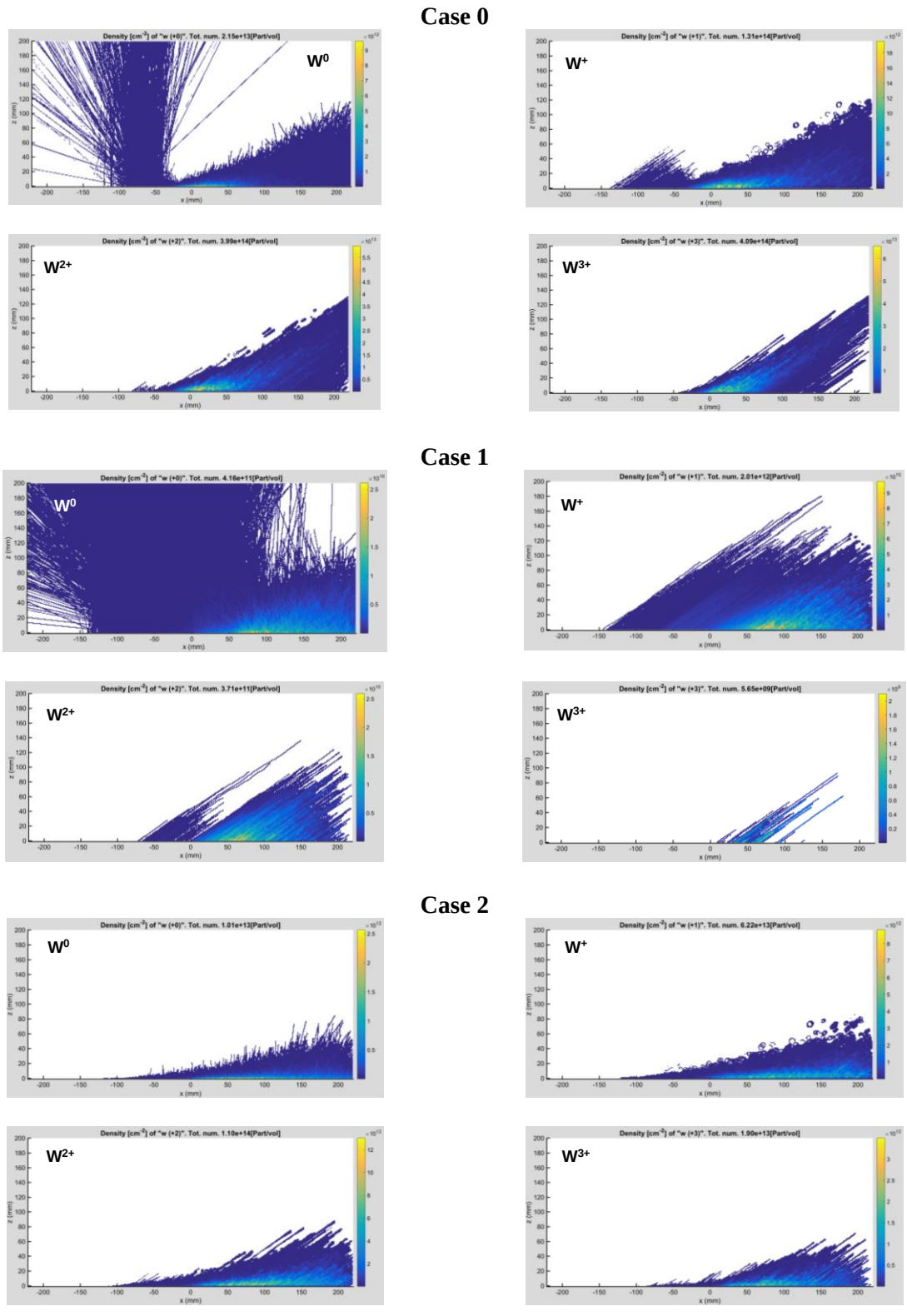


***Figure 19*** *2D distribution of tungsten atoms and charged ions for the 3 inner divertor cases. The colour bars are in arbitrary units.*

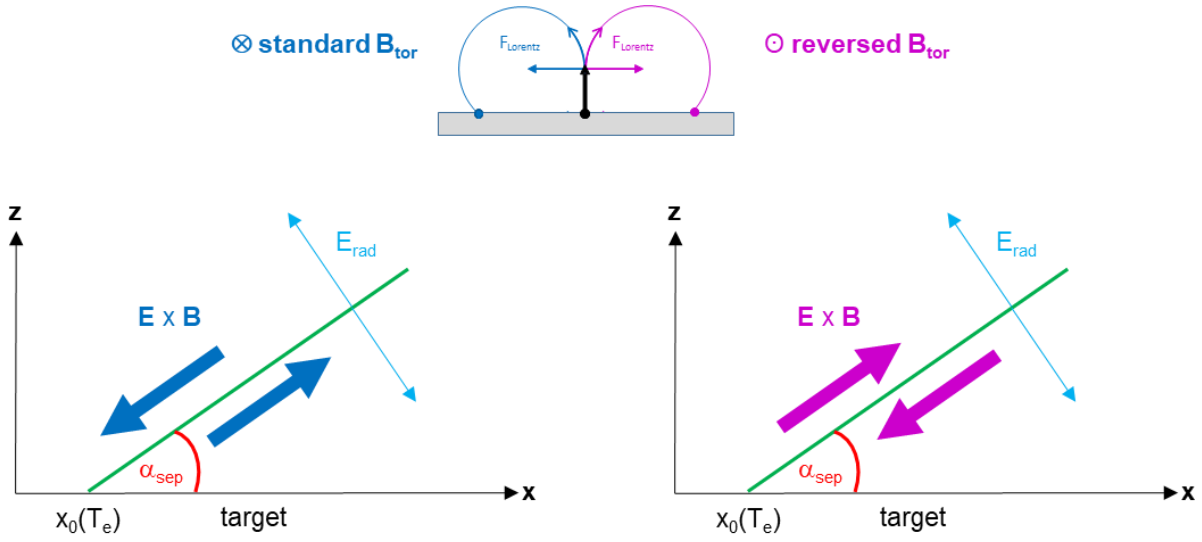


***Figure 20*** *E×B drift direction caused by the radial electric field $E_{rad}$ within the SOL and PFR of the inner divertor for reversed and standard magnetic field direction. On top of the figure the direction of the ion gyration is shown for both cases.*

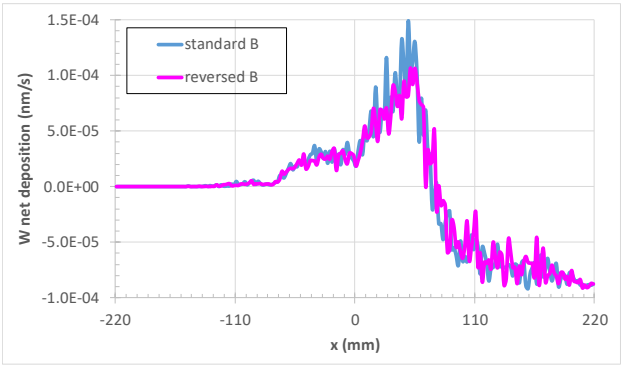


***Figure 21*** *Profiles of net tungsten deposition/erosion profiles along the inner divertor target for case 1 without anomalous cross-field diffusion: standard B versus reversed B field direction.*

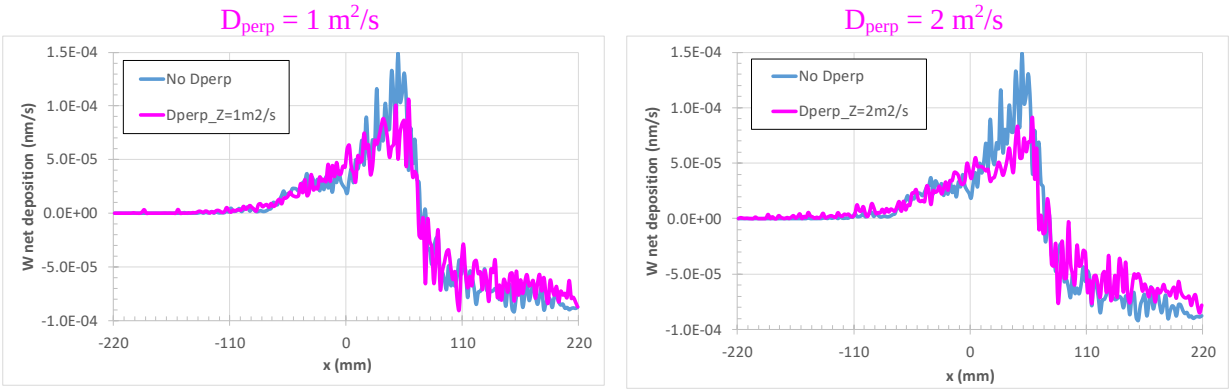


***Figure 22*** *Profiles of net tungsten deposition/erosion along the inner divertor target for case 1 with standard B field direction: study of the anomalous cross-field diffusion coefficient* $D_{perp}$.

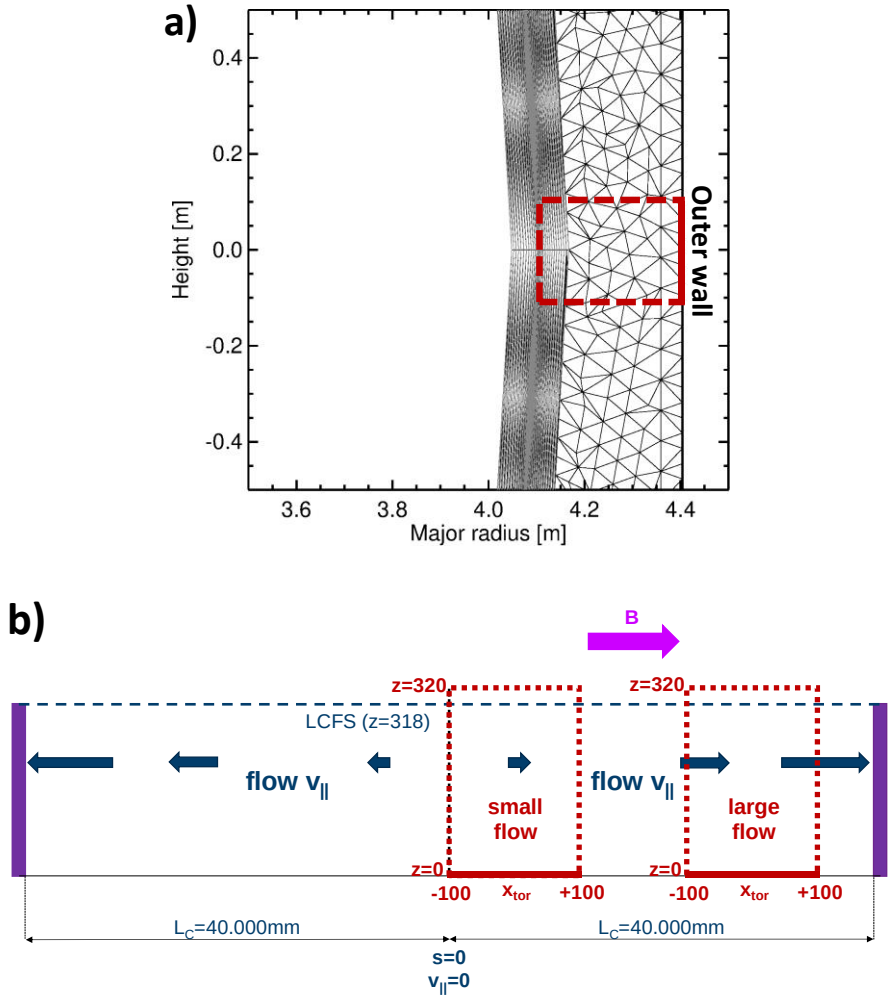


***Figure 23 a)*** *Poloidal cross section of the outer midplane region of STEP. The red dashed rectangular corresponds to the ERO simulation volume.* ***b)*** *Set-up of the ERO simulations for the cases of small and large background plasma flow. The x-coordinate corresponds to the toroidal direction, the z-coordinate to the major radial direction of STEP.*

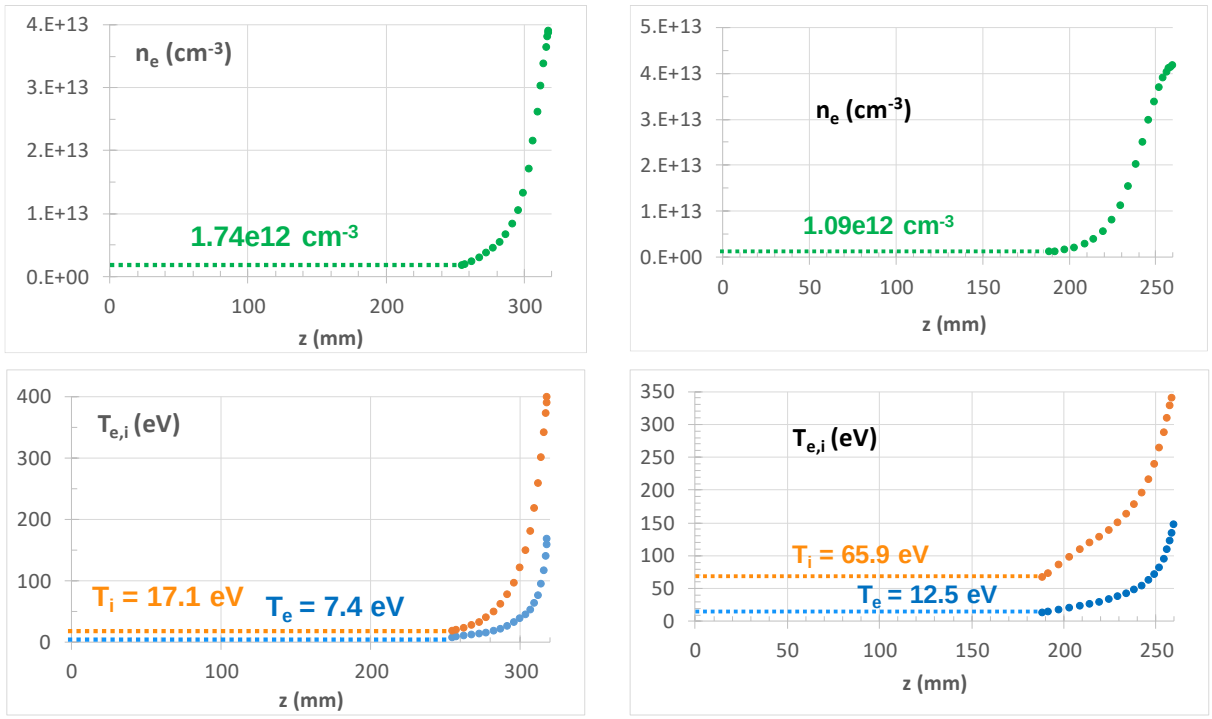


***Figure 24*** *Radial plasma parameter profiles for the ERO midplane simulations, the z-coordinate is along the major radius with z = 0 at the wall.* ***Left:*** *outer midplane.* ***Right****: inner midplane. The data points correspond to the SOLPS data, the dashed lines indicate the constant extrapolation towards the wall.*

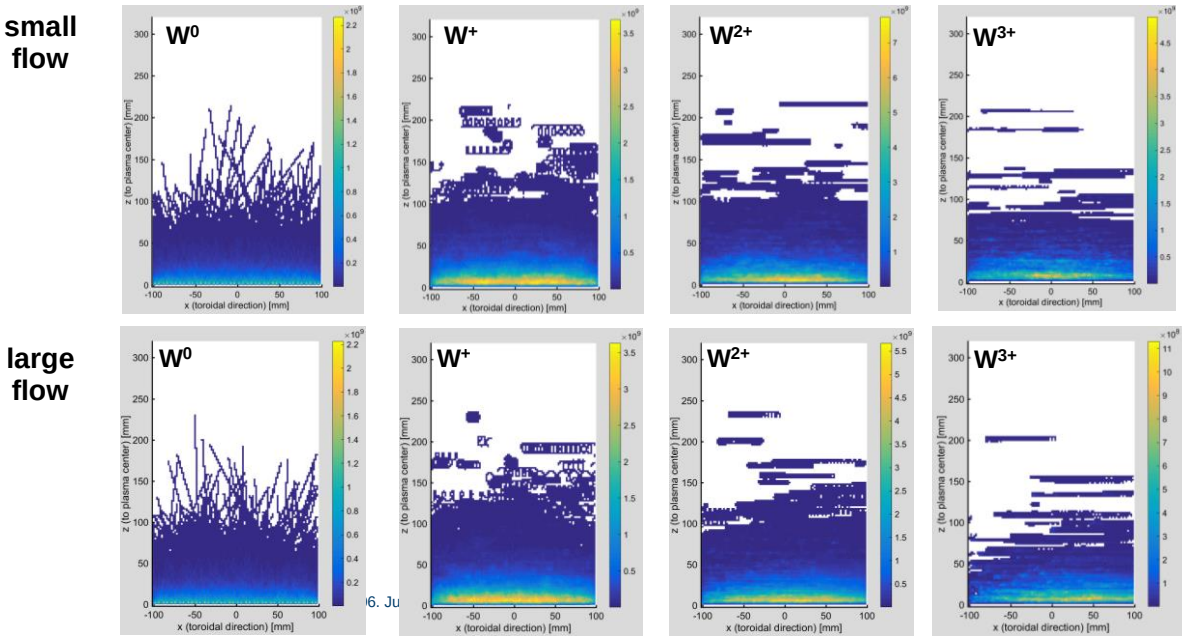


***Figure 25*** *Tungsten distribution (in [a.u.]) of atoms and various ions above the outer midplane surface integrated along the poloidal direction: "small flow" vs. "large flow" assumption for the parallel background velocity.*

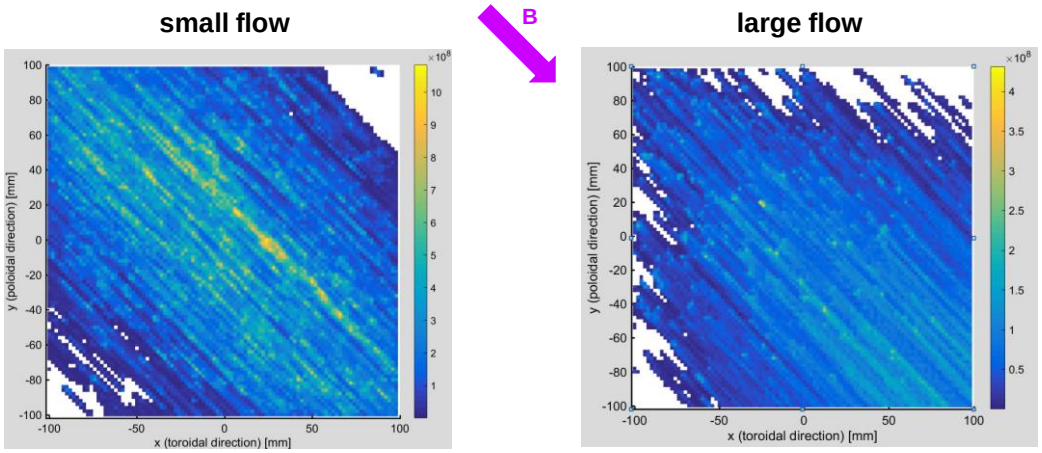


***Figure 26*** *Distribution (in [a.u.]) of $W^{3+}$ ions above the outer midplane surface integrated along the radial direction: "small flow" vs. "large flow" assumption for the parallel background velocity. The parallel background velocity is directed parallel to the B field direction.*

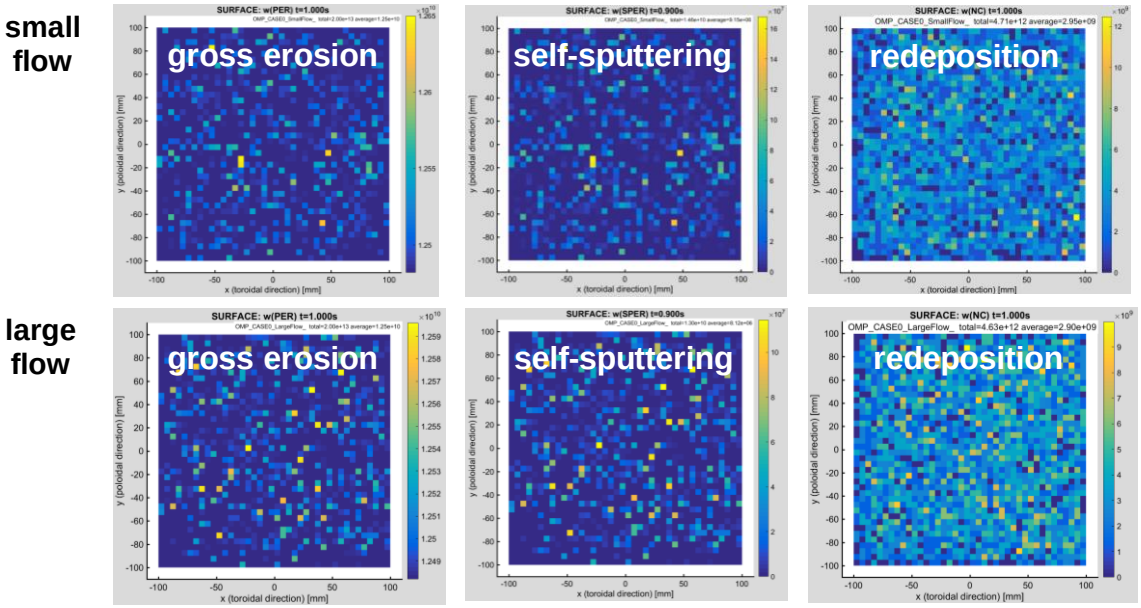


***Figure 27*** *Simulated gross erosion, self-sputtering and deposition on the outer midplane tile for small and large background flow velocity. Colour scaling: number of W atoms per mm$^2$ and 0.1s.*

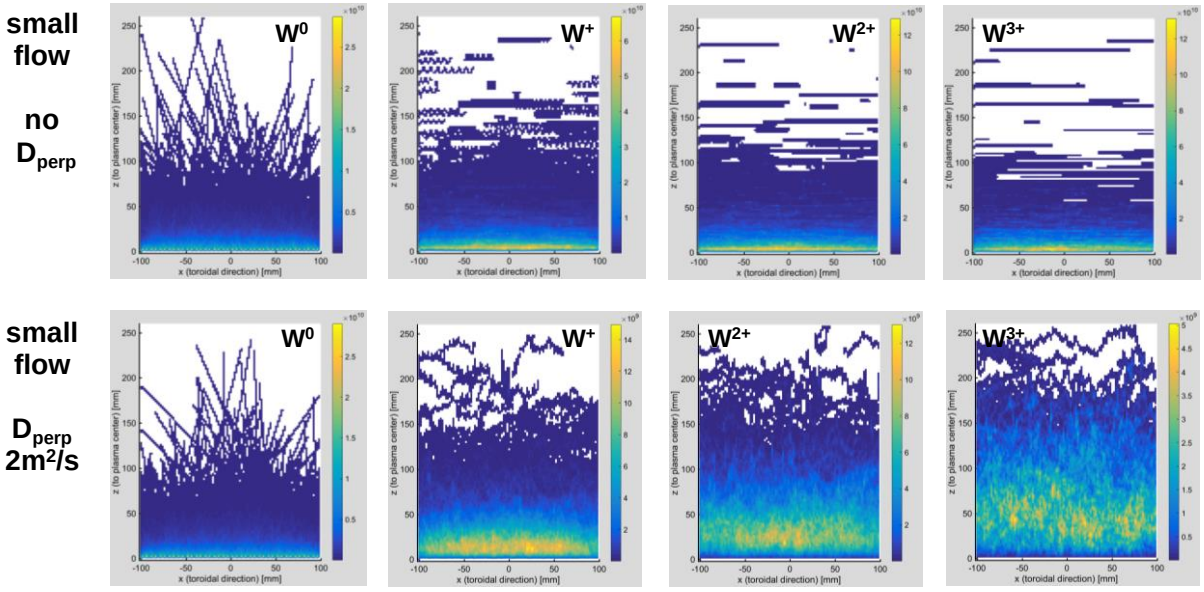


***Figure 28*** *Tungsten distribution (in [a.u.]) of atoms and ions above the inner midplane surface integrated along the poloidal direction for the small flow case: influence of the anomalous cross-field diffusion.*

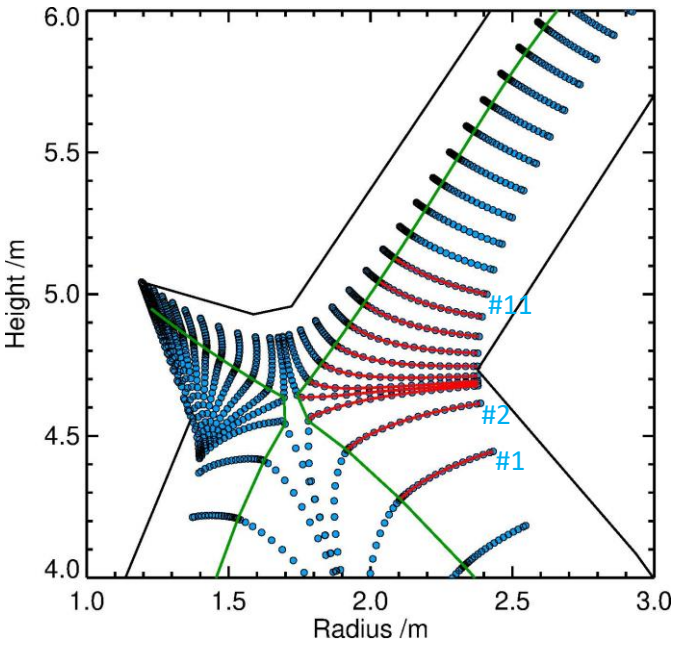


***Figure 29*** *Poloidal cross section of the upper part of STEP including the SOLPS grid. 11 grid points, indicated in light blue, are used for the gross erosion estimations at the outboard baffle entrance.*

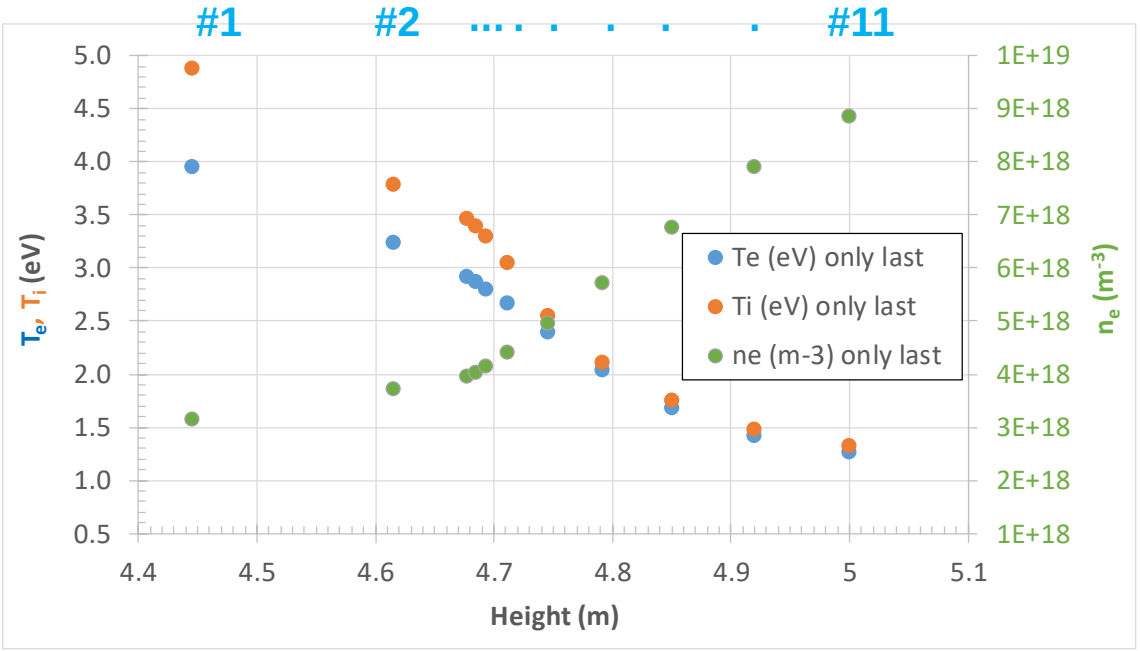


***Figure 30*** *Plasma parameters corresponding to the 11 grid points as indicated in figure 30.*

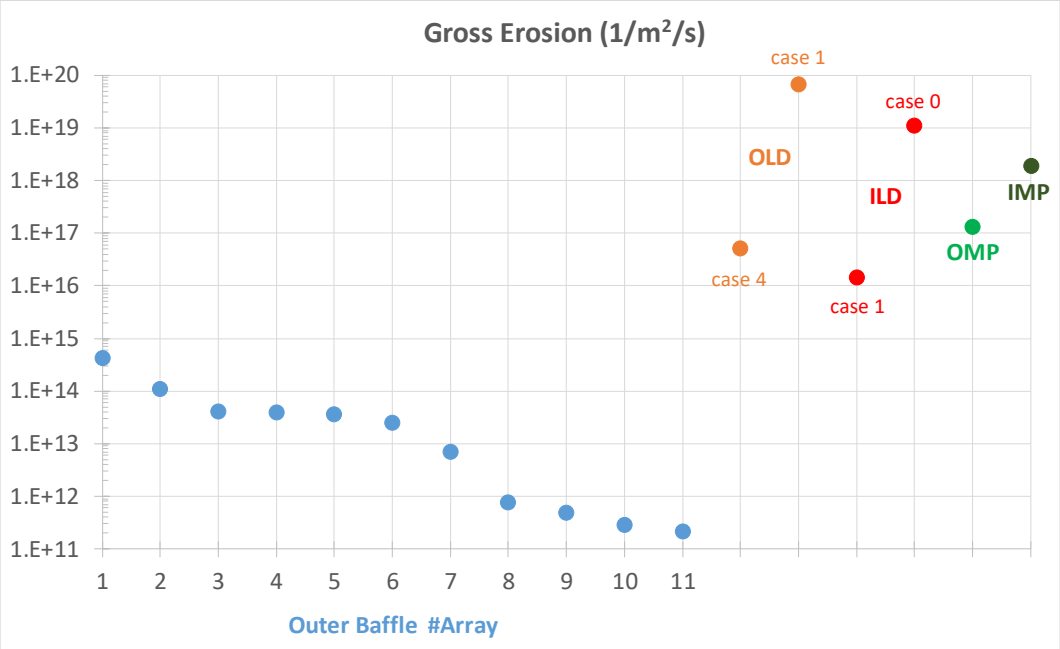


***Figure 31*** *Comparison of calculated tungsten gross erosion fluxes: ILD - inner lower divertor, OLD - outer lower divertor, OMP - outer midplane, IMP - inner midplane. For the divertor the minimum and maximum of the peak values values are provided according to the various plasma cases and parameter variations studied.*

## Tables

| | Case 1 | Case 2 | Case 3 | Case 4 | Case 5 |
|---|---|---|---|---|---|
| **$T_e$ /eV** | 6.6 | 4.6 | 8.9 | 11.2 | 26.1 |
| **$T_i$ /eV** | 12.5 | 7.74 | 12.1 | 17.1 | 27.7 |
| **$n_e$ /1E14cm$^{-3}$** | 7.2 | 8.0 | 7.7 | 5.9 | 4.3 |
| **$\lambda_{Te}$ (PFR) /mm** | 84 | | | | |
| **$\lambda_{Te}$ (SOL) /mm** | 69 | | | | |
| **$\lambda_{Ti}$ (PFR) /mm** | 90 | | | | |
| **$\lambda_{Ti}$ (SOL) /mm** | 56 | | | | |
| **$\lambda_{ne}$ (PFR) /mm** | 29 | | | | |
| **$\lambda_{ne}$ (SOL) /mm** | 97 | | | | |
| **$Ar^+$ /%** | 2.0 | 0.26 | 0.6 | 0.005 | 0.12 |

***Table 1*** *Peak values of the plasma parameters at the outer divertor target, exponential decay lengths for the plasma parameter fits towards PFR and SOL and Ar concentration.*

| | Case 1 | Case 2 | | | Case 3 | Case 4 | Case 5 | | |
|---|---|---|---|---|---|---|---|---|---|
| **$D_{perp}$ ($m^2$/s)** | 0 | 0 | 1 | 2 | 0 | 0 | 0 | 1 | 2 |
| **Peak Gross Erosion (1E19 atoms/$m^2$/s)** | 6.7 | 0.031 | 0.031 | 0.031 | 3.3 | 0.005 | 2.4 | 2.2 | 2.1 |
| **Deposition (%)** | 96.9 | 92.9 | 96.1 | 96.7 | 98.4 | 83.2 | 90.6 | 93.7 | 95.4 |
| **Prompt Deposition (%)** | 89 | 82 | 88 | 92 | 94 | 75 | 88 | 92 | 94 |
| **Self-Sputtering (%)** | 39 | 27 | 13.7 | 11.2 | 46 | 26 | 34 | 13.3 | 10.4 |
| **Peak Net Erosion (nm/s)** | 0.3 | 0.003 | 0.002 | 0.001 | 0.15 | 5E-4 | 0.15 | 0.1 | 0.06 |

***Table 2*** *Summary of erosion and deposition characteristics of the 5 cases for the outer divertor target. For case 2 and case 5 also results with non-zero $D_{perp}$ are included.*

| | Case 0 | Case 1 | Case 2 |
|---|---|---|---|
| **$T_e$ /eV** | 8.4 | 2.7 | 6.7 |
| **$T_i$ /eV** | 54.6 | 5.8 | 14.5 |
| **$n_e$ /1E14 cm$^{-3}$** | 13.8 | 11.1 | 11.1 |
| **$\lambda_{Te}$ (PFR) /mm** | 60 | 125 | |
| **$\lambda_{Te}$ (SOL) /mm** | 124 | 900 | |
| **$\lambda_{Ti}$ (PFR) /mm** | 65 | 94 | |
| **$\lambda_{Ti}$ (SOL) /mm** | 200 | 10000 | |
| **$\lambda_{ne}$ (PFR) /mm** | 36 | 36 | |
| **$\lambda_{ne}$ (SOL) /mm** | 20 | 33 | |
| **$Ar^+$ /%** | 0.25 | 1.2 | 1.0 |

***Table 3*** *Peak values of the plasma parameters at the inner target, exponential decay lengths for plasma parameter extrapolation in the inner divertor and Ar concentrations.*

| | Case 0 | Case 1 | | Case 2 |
|---|---|---|---|---|
| **$D_{perp}$ (m$^2$/s)** | 0 | 0 | 1 | 2 | 0 |
| **Peak Gross Erosion (1E19 atoms/m$^2$/s)** | 1.1 | 0.0014 | 0.0014 | 0.0014 | 0.22 |
| **Deposition (%)** | 98.6 | 88.2 | 88.6 | 89.2 | 98.6 |
| **Prompt Deposition (%)** | 30 | 5 | 11 | 15 | 29 |
| **Self-Sputtering (%)** | 13 | 9.3 | 3.6 | 3.0 | 10.7 |
| **Peak Net Erosion (nm/s)** | ~0.04 | ~1E-4 | ~8E-5 | ~7E-5 | ~0.01 |

***Table 4*** *Summary of erosion and deposition characteristics of the 3 cases for the inner divertor target. For case 1 also results with non-zero $D_{perp}$ are included*

| | $T_e$ (eV) | $T_i$ (eV) | $n_e$ (cm$^{-3}$) | $D^+$ flux (1/m$^2$/s) | Y ($D^+$ on W) | Y ($Ar^+$ on W) |
|---|---|---|---|---|---|---|
| **outer midplane** | 7.4 | 17.1 | 1.74E12 | 1.0E21 | 6.0E-7 | 1.2E-2 |
| **inner midplane** | 12.5 | 65.9 | 1.09E12 | 1.2E21 | 8.8E-5 | 1.6E-1 |

***Table 5*** *Plasma parameters and resulting sputter yields at the outer and inner midplane tiles.*

| | | small flow | | large flow | |
|---|---|---|---|---|---|
| | | OMP | IMP | OMP | IMP |
| **Gross Erosion** | **no $D_{perp}$** | 1.3E17 W/($m^2$s) | 1.9E18 W/($m^2$s) | 1.3E17 W/($m^2$s) | 1.9E18 W/($m^2$s) |
| | **$D_{perp1}$** | | | | |
| | **$D_{perp2}$** | | | | |
| **Deposition** | **no $D_{perp}$** | 23.6% | 11.6% | 23.2% | 11.2% |
| | **$D_{perp1}$** | 52.5% | 52.8% | 51.5% | 51.8% |
| | **$D_{perp2}$** | 58.5% | 58.6% | 57.5% | 59.3% |
| **Prompt Deposition** | **no $D_{perp}$** | 22.3% | 11.1% | 22.1% | 10.7% |
| | **$D_{perp1}$** | 30.6% | 21.5% | 30.9% | 20.9% |
| | **$D_{perp2}$** | 36.3% | 26.2% | 35.8% | 26.6% |
| **Self-Sputtering** | **no $D_{perp}$** | 0.06% | 0.3% | 0.06% | 0.3% |
| | **$D_{perp1}$** | 0.05% | 0.6% | 0.05% | 0.5% |
| | **$D_{perp2}$** | 0.04% | 0.6% | 0.05% | 0.6% |

***Table 6*** *Gross erosion rates and amounts of deposition, prompt deposition and self-sputtering at the outer midplane (OMP) and inner midplane (IMP) tile. $D_{perp1}$ = 1 $m^2$/s and $D_{perp2}$ = 2 $m^2$/s.*

| Grid point | $T_e$ (eV) | $T_i$ (eV) | $n_e$ ($cm^{-3}$) | $D^+$ flux (1/$m^2$/s) | Y ($D^+$ on W) | Y ($Ar^+$ on W) | Gross Erosion (1/$m^2$/s) |
|---|---|---|---|---|---|---|---|
| #1 | 3.94 | 4.88 | 3.12E+12 | 1.11E+21 | 0 | 3.75E-05 | 4.21E+14 |
| #2 | 3.23 | 3.78 | 3.69E+12 | 1.17E+21 | 0 | 9.12E-06 | 1.08E+14 |
| #3 | 2.91 | 3.45 | 3.94E+12 | 1.19E+21 | 0 | 3.39E-06 | 4.09E+13 |
| #4 | 2.86 | 3.38 | 4.02E+12 | 1.21E+21 | 0 | 3.15E-06 | 3.84E+13 |
| #5 | 2.79 | 3.29 | 4.14E+12 | 1.23E+21 | 0 | 2.87E-06 | 3.55E+13 |
| #6 | 2.66 | 3.04 | 4.40E+12 | 1.26E+21 | 0 | 1.93E-06 | 2.46E+13 |
| #7 | 2.39 | 2.54 | 4.93E+12 | 1.31E+21 | 0 | 5.28E-07 | 7.00E+12 |
| #8 | 2.03 | 2.10 | 5.69E+12 | 1.39E+21 | 0 | 5.41E-08 | 7.59E+11 |
| #9 | 1.67 | 1.75 | 6.74E+12 | 1.50E+21 | 0 | 3.21E-08 | 4.85E+11 |
| #10 | 1.41 | 1.47 | 7.89E+12 | 1.61E+21 | 0 | 1.75E-08 | 2.83E+11 |
| #11 | 1.26 | 1.32 | 8.84E+12 | 1.70E+21 | 0 | 1.24E-08 | 2.13E+11 |

***Table 7*** *Plasma parameters at the outboard baffle entrance, according tungsten sputter yields and resulting tungsten gross erosion fluxes.*